Thesis for the Degree of
Master of Science

INVESTIGATION OF THE GROWTH PROCESS OF SILICON FROM THE GAS PHASE IN THE DYNATEC CENTRIFUGE AND FREE SPACE REACTOR

by
AIDAN VON BONIN

University of Oslo

Department of Physics
Centre for Materials Science and Nanotechnology (SMN)

1st June 2015

UiO : Faculty of Mathematics and Natural Sciences
University of Oslo

Preface

This thesis is submitted for the degree of Master of Science as the final part of my Master's degree in the program Materials Science and Nanotechnology (Materialer, Energi og Nanoteknologi) of the Physics department at University of Oslo.

The production and study of samples from the Free Space Reactor and the Dynatec Centrifugal Reactor is a part of FME SOL Work Package 7. This work was performed in order to evaluate techniques for the characterisation of the products and to gain deeper understanding of the mechanisms involved. The work done in this thesis was in close cooperation with the Institute for Energy Technology (IFE) in Kjeller, Norway; there, all samples were produced and the X-Ray diffraction experiments carried out.

I would like to thank Anette E. Gunnæs and Martin Kirkengen for the opportunity to conduct this work and for thoughtful guidance and supervision during the whole period.

I acknowledge the whole Structure Physics group for the great time I had during my master studies. I learned a lot from you, had great dialogues and fruitful conversations. I am specially grateful for Phuong Nguyen for training me in the equipment, most importantly the TEM. Thank you to Ole Bjørn Karlsen and Øystein Prytz for helpful hints and discussions and Raluca Tofan for great conversations during the whole time. Thank you to Werner O. Filtvedt and the team at IFE involved with the sample production and XRD measurements for the input and support. This was a great help for the success of this project. To my fellow master students: you are great, it was a pleasure spending time with you.

Special thanks to Linda Hammervold for reading through this work and pointing out some grievous syntax and spelling mistakes.

Last but not least thanks also to my friends who were able to stand me, especially during the last weeks of my master. And to my family, your support means everything to me.

Aidan von Bonin

University of Oslo, May 2015

Abstract

Silicon is by far the most important semiconductor for use in electronic- and photovoltaic applications. As a result from policy changes in countries such as Germany, Japan and others the installation of photovoltaic modules increased rapidly in the beginning of the last decade. This led to a short sale on the photovoltaic market. However after China entered the market, flooding it with cheap modules, many producers were pushed out of the marked as they could no longer compete with the low prices. This price drop encouraged producers to investigate new, less energy consuming process methods for silicon production.

In this masters thesis the results of two such methods are discussed with respect to production processes on the microscopic scale. Samples from a Dynatec Centrifuge Reactor (DCR) and a Free Space Reactor (FSR) were analysed using visible light and electron microscopes as well as electron and X-Ray diffraction. The results suggest a strong dependence of the formation of crystallised structures on temperature. Phosphorous doping, however, can reduce this temperature. The major part of particles produced in the FSR at 575 °C and below grew to a size between 50 and 200 nm and were predominantly amorphous. At 600 °C the size and the fraction of crystalline particles grew significantly.

The location within the DCR has a major effect on the density, crystallinity and hardness on the end product. The wall area shower crystalline silicon, the ceiling amorphous and crystalline structures and the exhaust almost only amorphous particles. The change of silane content within the reaction gas inside the reactor is one of the reasons for this change.

The effect of carbon contamination on the growth process and the end product has been investigated. It has been found that it influenced the homogeneous growth and led to a diverse end product. Areas with no Carbon whatsoever, as well as those with crystalline Carbon, graphite and SiC structures were found.

Contents

List of Figures

List of Tables

1. Theory

1.1 Introduction

Silicon (Si) is with about 27.7 % the second most abundant chemical element in the earth's crust, after Oxygen (O) [1]. Thus the accessibility of the raw material is in most aspects unlimited.

In computer technology it has been the single most important material as it provides practically all electronics nowadays used with semiconductor and solid state elements. Another, even bigger field for applications, by volume, is the use for photovoltaic modules to harvest sunlight in order to produce electricity.

Since the production of high purity silicon is a rather energy intensive process facilities for production and refining are located close to energy sources. In Norway, these source are mainly water power plans. Such facilities are constructed close to rivers and streams, often near the coast or fjords. The abundance of cheap energy is the main reason why so many energy-intensive plants such as aluminium and silicon production facilities were built in Norway.

Due to the recent development in renewable energy policies, the demand of solar cells increased exponentially. Since silicon solar cells take about 90 % of the world solar cell market, the need for solar cell grade silicon increased significantly. This high demand led to a shortage and consequently high prices. This again triggered a massive production expansion mostly in China. As a consequence, the global price for solar cell grade silicon dropped and many producers that could not keep up with the prise drop were pushed out of the market. Norwegian silicon producers felt this increased pressure which led to the development of new and less energy consuming production processes.

1.2 Historical Background

In the beginning of the 20th century companies such as Elkem invented and developed processes for ferroalloy and aluminium production. Since solar-cell silicon is a refined product of metallurgical silicon, it is very closely related to the metallurgical industry in Norway. The first producers in Norway were companies with a rather widespread product portfolio,

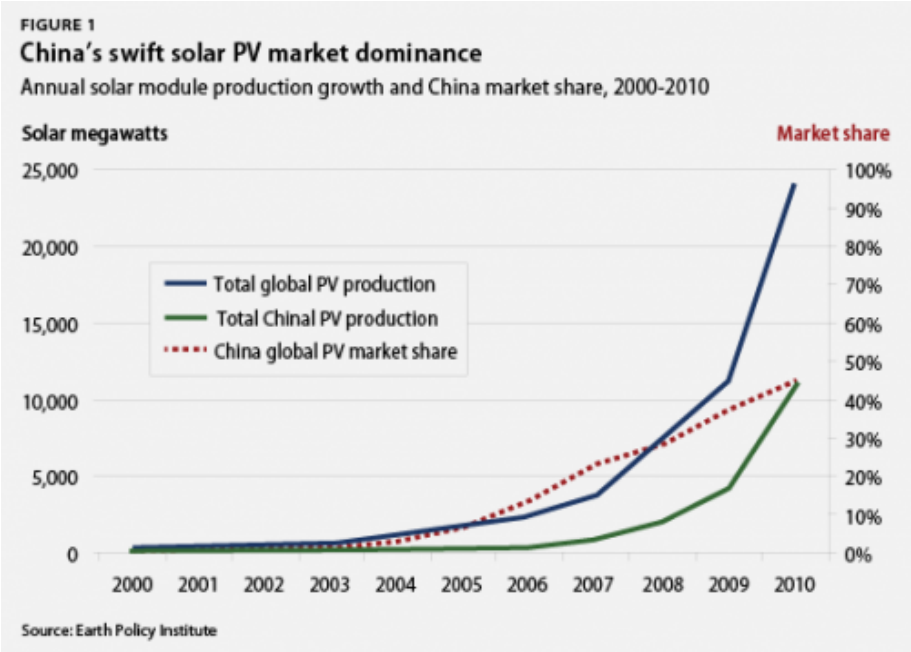

Figure 1.1: Development of China's solar cell production [2]

covering a broad spectrum of products. However, Throughout the years the all-rounders changed from generalists to specialist, thus they focussed, in this case, on silicon production. In the 1960s the Norwegian semiconductor and microelectronics industry started up opening a new market in Norway for silicon and silicon products. In the 1990s and beginning of 2000s Norwegian Solar cell production started up with a series of companies using the cheap and abundant hydro power in Norway. At first the target was to produce small, high priced off-grid Photo Voltaic (PV) systems that are not depending on subsidies. However, the picture changed when policies in Germany, Japan and other countries guaranteed heavy subsidies for private PV installations which triggered a massive demand for both solar grade silicon and solar cells.

At that time the China's silicon production was still not in place, leaving the marked to producers in Europe and North America. At the end of the 2000s however Chinas solar cell industry flooded the market with cheap modules and thus increasing the pressure on other producers and pushing them out of the market.

1.2.1 Price development

The price development of silicon is closely linked to the prices of solar cells, as they are the main products when it comes to volume. Nevertheless, changes in policies, research and development in solar cell technology and, not to mention the growth of the solar cell industry have caused a price decline resulting in prices of silicon solar cells below $1 per watt. Figure 1.2 presents the price development of the last decades. It can be seen that

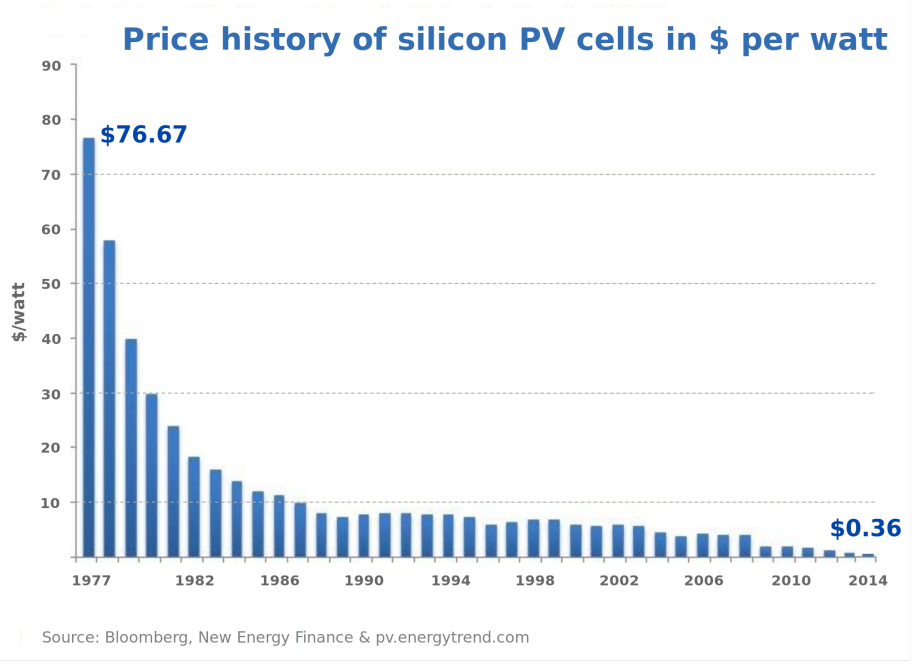

Figure 1.2: Price development of silicon solar cells during the past decades [3]

the prices are very stable just below $10 throughout the 1990s until the beginning of the 2000s. This learning curve for solar cells is widely known and recited.

An interesting feature however, can better be seen in figure 1.3, where the module price is logarithmically plotted against the global production volume. Specifically the increasing price in 2006 is to be mentioned. It can be seen that the market grew steadily until 2004 where it suddenly stopped. What happened here was that the market supply of solar cells silicon was lower than the demand. The big scale silicon production for PV was still not in place and large parts of the material used came from scrap Si from the semiconductor industry.

At this point, in 2004, the solar cell industry grew out of the value chain it had until this point. The market's reaction is slow as it takes some time to start new big scale factories to satisfy the market's demand. This is a major reason for increasing prices as seen in figure 1.3. At about that time, the International Energy Agency (IEA) estimated that the learning curve was flattening out and that there would not be that much more solar PV entering the market. However, with Chinese Si production in place in 2008, new silicon entered the market and the prices fell, levelling off into the previously interrupted curve. The plot shows that the Si production is so important that the whole market has been disturbed including future projections. [5]

Figure 1.4 visualizes the different reactors in the market, their production volume and the cost per kg of each of these methods. It is clear that

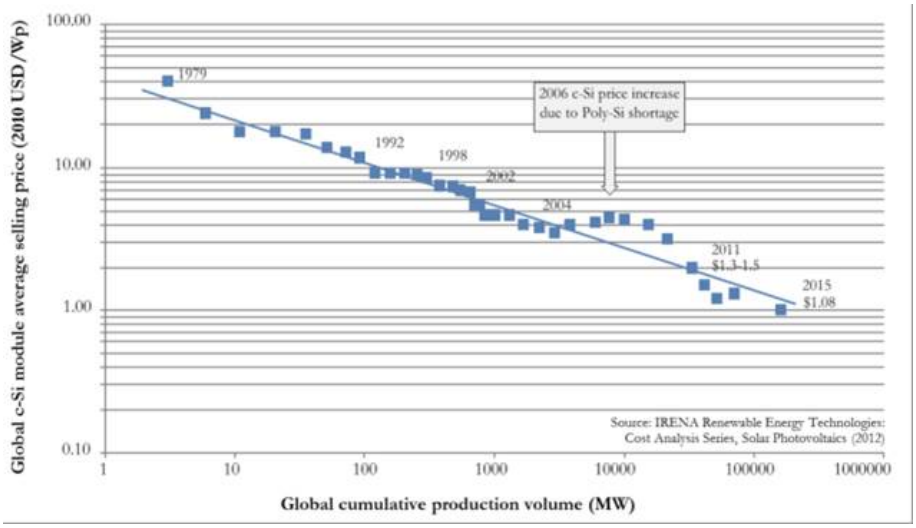

Figure 1.3: Price development of silicon solar cells on logarithmic scale [4]

the major part of silicon comes from the different types of Siemens reactors (v.i.). However, at the same time, these reactors require the highest market price. The technology on the very left side of the plot, producing to the lowest cost per kg, is the Fluidized Bed Reactor (v.i.). The reactors discussed in this work are expected to position themselves even further left.

To understand mechanisms involved in the production, and thus reduce the energy consumption even further, is the goal of this work.

1.2.2 Value creation chain in silicon production

Two ways to describe the value chain of silicon solar cells can be seen in figures 1.5 and 1.6. The first one approaches the topic by describing the flow from the raw material through all the stages to the end product. The second approach is from the financial side looking at the costs at each production stage and evaluating them with respect to the overall costs. It appears that the largest single group of costs is in the refining of the raw silicon to produce pure polysilicon. This is part of the upstream process and is handled by the Silicon-industry (cf. figure 1.5).

The materials analysed in this work are from the largest part. In the context of this thesis the raw material is monosilane gas and the product is pure polysilicon. This material is purified but does not have as high standards as demanded by the computer industry. The lowest requirements for the semiconductor industry is 9N purity (99.9999999 % Si) while for Si used in solarcells it has to be at least 6N purity [9].

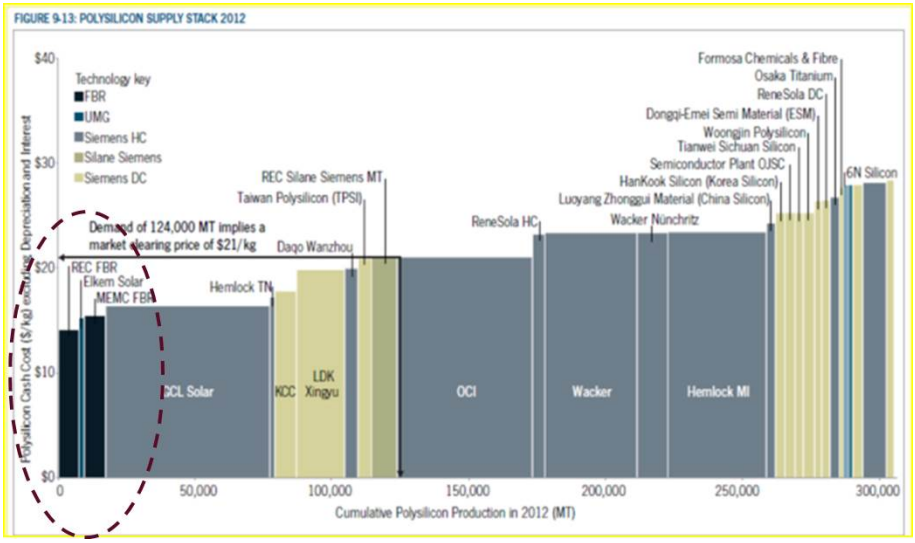

Figure 1.4: The figure shows the price of each polysilicon supplier in 2012 with respect to the production volume and relative to each other [6]

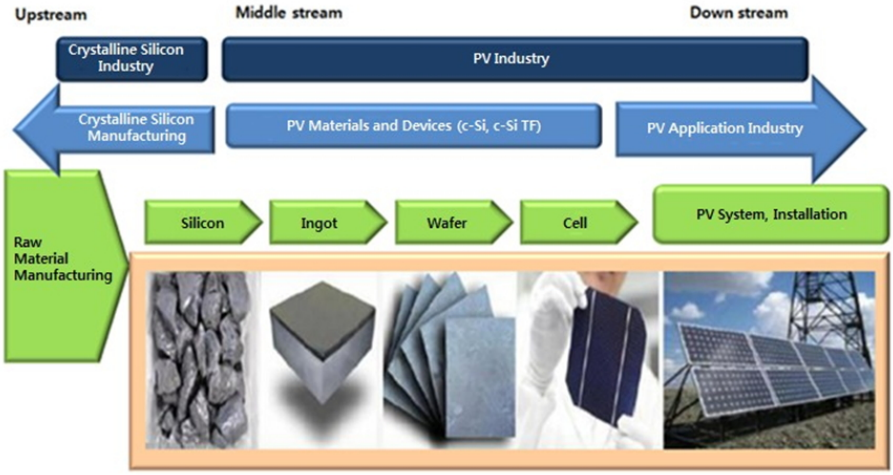

Figure 1.5: Supply chain for silicon solar cells [7].

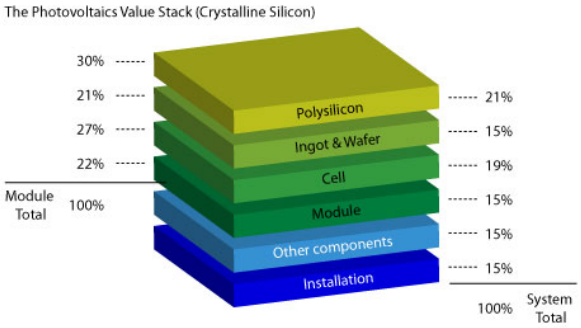

Figure 1.6: Supply stack for solar cells silicon [8].

1.3 The reactors

Silicon is a widely studied material. Especially due to the extensive usage in computer technology with its high demands in terms of purity, plenty of research has been done and a huge body of literature is available. The specific topic of silicon production from trichlorosilane (TCS) and monosilane (silane) in CVD reactors has also been researched, and new attempts are being made in order to develop production methods that reduce the total energy consumption of the process. It appears that Norway is host to some of the leading companies in this field with developments in FBR as seen in figure 1.4, page 5.

Two main routes for producing solar cell grade silicon can be specified: through metallurgy and via the gas phase, using Chemical Vapour Deposition (CVD). This work focusses solely on the second route. The reactant gases, either TCS or silane, decompose at high temperature leaving behind solid Si and waste and exhaust (v.i.). Besides low energy consumption and high quality of the end product, the yield is a very important factor in significantly effecting the value chain. One significant contribution to the yield is the control of fines production in the process. Fines are small Si-particles that are so light that they leave the reactor through the exhaust and are thus not available as an end product. Fines are seen as a loss in the process and a reduction of those particles increases the yield significantly. Its properties with regards to reactivity and smelting is rather different than the original product, which makes it problematic to sell and thus it is not desirable. The high reactivity might come from the large surface to bulk ratio, so they react with whatever reactive environment they are exposed to.

Fines production is an issue in reactors where large particles or bulk Si is produced. The size of these particles is approximately the same as the end product of the Free Space Reactor (FSR) (v.i.).

The decomposition of silicon containing gas such as TCS and silane is briefly discussed by Filtvedt [10]. The author describes working temperatures for Siemens reactors running with TCS up to 1100 °C to increase the yield and get a high quality product. Theoretically the decomposition temperature of TCS is 468 °C but the formation of higher order chlorosilanes and problems with chlorine contamination requires more heat [11]; chlorine is highly unwanted. It also appears that Silicon has favourable electrical properties at that high temperature. Switching to Fluidized Bed Reactor (FBR) has the major benefit not to be dependent on electrical conductivity. Thus the temperature can be reduced to 850 - 1050 °C for TCS.

$$2HSiCl_3 \Longrightarrow Si + 2HCl + SiCl_4 \tag{1.1}$$

The use of TCS results in emission of exhaust hazardous hydrochloric acid (HCl), as it can be seen in equation 1.1 where $HSiCl_3$ is the chemical formula of TCS and $SiCl_4$ refers to tetrachlorosilane.

$$SiH_4 \Longrightarrow Si + 2H_2 \tag{1.2}$$

Equation 1.2 shows the thermally decomposition of monosilane into silicon and hydrogen; SiH_4 is the chemical formula of monosilane. The theoretical decomposition temperature is 420 °C.

In an attempt to reduce the energy usage as a major cost factor of the silicon production, private companies and research institutes have developed different techniques to produce silicon. Several techniques are presented here. A common factor of all presented techniques is the use of silane gas as a precursor, instead of TCS. So far the prices are not as high due to the lower competition for this chemical, as there is less competence for large scale silane production. The main reason for using silane as a reactant gas is, however, the lower decomposition and deposition temperature and therefore reduced energy consumption.

1.3.1 Particle growth

Particle growth from the gas phase is a widely used technology e.g. for the production of black carbon, an important raw-material in various industry processes and products.

F. C. Eversteyn and Peek has reported the usage of monosilane for the growth of epitaxial Si. It was observed that when the silane concentrations were increased to increase the growth rate, fine particles are formed in the gas phase [12]. This behaviour has been utilized by Murthy et al. to form fine particles in size 300 - 800 Å in high temperature (1000 °C) directly from the gasphase. The particles proved to be crystalline, the dominating growth mechanism was the diffusion controlled growth. It has been shown that the yield increased with temperature and the growth of the particles was epitaxial [13].

The process of gas to powder conversion has been studied as well by Kusters and Pratsinis [14]. The authors distinguish between coagulation- and condensation controlled particle formation from the gas phase where the first case results in agglomerate powders. In the second case non-agglomerate powders are produced. The authors define coagulation as the particle growth due to collision with product molecules, whereas in condensation the particle growth is by means of collision with other particles. Kusters and Pratsinis conclude that when particle formation takes place by uninhibited chemical reaction, mechanisms favour coagulation controlled particle growth resulting in agglomerates of solid primary particles.

In her thesis Giesen models and simulates the synthesis of nano particles from the gas phase [15]. The author describes the pyrolysis of a gas; after the decomposition the product is still in the gas phase and forms a particle as soon as the system is supersaturated. The particle growth is described as mainly diffusion driven, where two cases are discussed: a system below the melting temperature where diffusion happens on the surface, along the grain boundaries or through the volume. The second

case discusses a system near the melting point. Here, the evaporation and condensation processes gain importance. The processes are differentiated between fast and slow coalescence depending on the coagulation time relative to the sinter time. In case the sinter time much longer than the coagulation time, the author speaks of fast coalescence where spherical particles are being formed. In the other extreme case where the coagulation time is much longer than the sinter time, agglomerates are formed. The author models the process where fine particles grow during coalescence from small to big particles. Here few small spheres form together larger particles. Those again attach with others in a next step and end up in one big sphere.

1.3.2 The Siemens Process

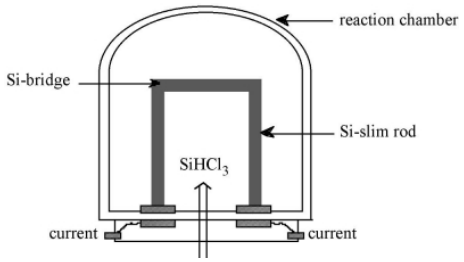

Figure 1.7: Drawing of the Siemens reactor process [16].

The major part of the world solar cell grade silicon production is nowadays produced using the so-called Siemens process. Here TCS gas is thermally decomposed in CVD and deposited on heated high-purity Si-rods as shown in figure 1.7. Advantages of this process are a high purity end product and a well known, understood and controlled process.

However, among the many disadvantages are low energy efficiency, low silane utilization and a non continuous, labour and equipment intensive process.

Nonetheless it is possible to run Siemens reactors with monosilane [17] and it is done [18]. But, as stated before, very big factories are necessary in order to produce silane at reasonable prices, and they are few in number.

1.3.3 Fluidized Bed Reactor

In the FBR seed particles are led into the reactor chamber. Through the bottom of the chamber, reaction gas is led together with fluidization gas into the chamber to keep them floating until they reach a certain size. This can be seen in the schematic drawing in figure 1.8. The fluidization gas is used to keep particles from sticking and adhering to the floor. When a critical size is reached, the particles exit the chamber through an outlet in the bottom. Exhaust and fines leave through the top. In the heated part of the reactor the reaction gas decomposes and the silicon grows on the seed particles.

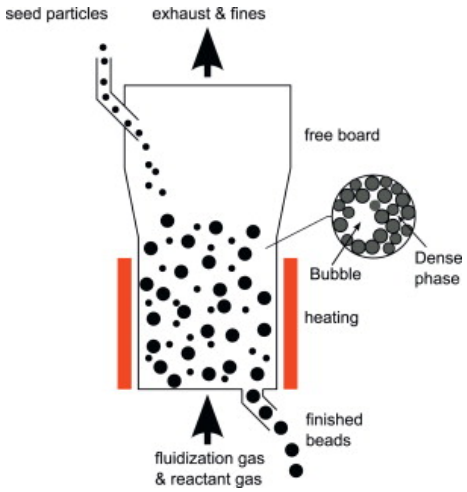

Figure 1.8: Drawing of the FBR [19].

Thus the particles grow, increase the weight and leave the reactor. Advantages of this type reactor is minimised heat loss and thus lower energy consumption compared to Siemens process. Also with this type of reactor, a continuous production is possible. Another great advantage of this process is the very large surface area of the particles within the reactor, so that the major part of the Si solidifies on the particles before the silane reaches the walls. The particles leaving the reactor have typically a seize in mm range.

1.3.4 Free Space Reactor

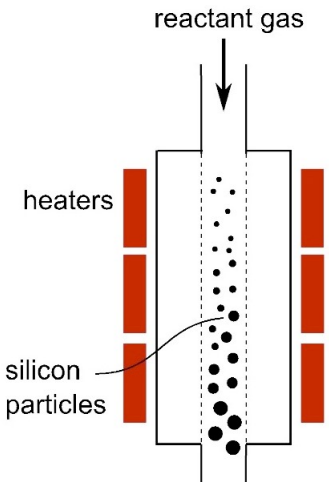

Figure 1.9: Drawing of the FSR [20]

Just like in the FBR in the Free Space Reactor (FSR) silane gas decomposes to silicon and hydrogen. Here, however, no seed particles are needed as they solidify directly from the gas phase to particles which then grow. The reactant gas flows continuously in a tube shaped

reactor (figure 1.9). Nonetheless, due to the laminar flow, both the silane concentration and velocity is higher in the centre of the tube. Thus close to the wall the silane concentration is lower and the particles stay longer e.g. in the heating zone.

In the heating zone, where the reaction is happening, the tube wall is perforated with inert gas flowing into the chamber to avoid attachment of the silicon onto the wall. Just as in the previous described reactor, the advantages are reduced heat loss and process continuity. In addition to that, the Institute for Energy Technology (IFE) has modified the system so that in-process doping of the silicon is possible. The Product of this process is a fine powder.

1.3.5 Dynatec Centrifuge Reactor

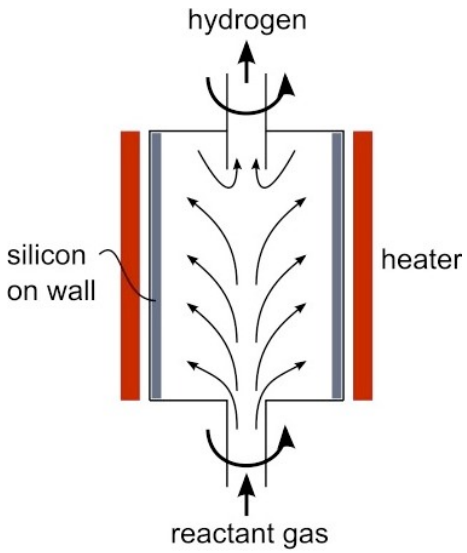

Figure 1.10: Drawing of the DCR [20]

The Dynatec Centrifuge Reactor (DCR) is, in contrast to the previous two described reactors non-continuous. Here, the reactant gas is led into a heated and rotating chamber where it is forced to the wall by the centrifugal force. The silane decomposes and solidifies on the wall (equation 1.2). Before the reaction gas is led into the reactor chamber, the wall is covered by a thin layer of small silicon particles to ensure easy removal of the product. The particles stay on the wall only by the rotational force [21].

As it can be seen in figure 1.10, the inlet of the gas is on the bottom of the reactor. It is then forced to the wall and by reaching the decomposition temperature, the Si production starts. The gas then rises up along the wall and due to constant decomposition it constantly decreases the fraction of silane in the gas mixture. The figure also shows that the heating is only on the wall area. The exhaust is located in the centre of the roof.

The samples used for analysis in this thesis were produced in the two last reactors.

2. Experimental

In the current study, samples from the FSR and the DCR have been investigated using various microscopy techniques combined with X-ray diffraction (XRD), electron diffraction (ED) and electron energy dispersive spectroscopy (EDS). Here the steps were first rather simple optical methods using two visible light microscopes (VLM) followed by scanning electron microscope (SEM) and transmission electron microscope (TEM) techniques.

All samples were produced by the IFE in Kjeller, Norway. They have been produced between September 2013 and February 2015.

2.1 Samples

For this work two different kind of samples from CVD reactors have been analysed. Firstly samples from varying sites within the DCR were analysed. The sites were: the reactor wall (crystalline, porous), the reactor roof (porous material) and the exhaust (powder). Secondly, powder samples from a FSR were analysed.

Regarding the nomenclature so are throughout this work, the samples referred to by the short names as they are defined in table 2.1 and 2.2. The short name consists of the first letter indicating the reactor type, the second letter indicating if the material is doped(p), carbon contaminated (c) or neither (i). The last part of the short name gives other information to distinguish the sample such as the temperature (in case of the FSR) or the position where the sample was taken from (DCR). The latter "r" indicates a repetition of a previous experiment.

Table 2.1: List of samples from the FSR

Sample ID	Short name	T_{max}	other elements
FSR-14.11.20	Fi600	600 °C	-
FSR-15.01.15	Fi575	575 °C	-
FSR-15.01.21	Fp575a	575 °C	P doping
FSR-15.02.03	Fp575b	575 °C	P doping
FSR-15.01.27	Fp525	525 °C	P doping

Table 2.2: List of samples from the DCR

Sample ID	Short name	T_{max}	other elements
D-13.09.25 wall top	Di-w-a	620 °C	-
D-13.09.25 roof	Di-r	620 °C	-
D-13.09.25 exhaust	Di-ex	620 °C	-
D-10 wall top	Dc-w-a	600 °C	carbon contaminated
D-10 wall bottom	Dc-w-b	600 °C	carbon contaminated

2.1.1 Sample Preparation

Depending on the kind of sample, different methods were used to prepare the samples. Crystalline materials were cut, ground and polished into thin slices. After mounting the approximately 10 μm thick sample on a copper ring the samples were ion milled so thin, that light could shine through. In some cases a small hole with rough edges was created. Porous materials were put into a copper tube (small pieces of the material, without crushing it) and filled with resin so that all air was removed. After it was cured the copper tube, about one mm long, was treated like the crystalline samples. The powder samples were dissolved in ethanol and one drop of the liquid was put on the holey carbon copper grid and dried.

2.2 Analysing Methods

2.2.1 Visible Light Microscopy

Visible light microscope is the simplest and quickest imaging method used to get a first look at the samples. It is used to get an overview of the sample and a first impression of the surface. The resolution of such microscopes is due to the wavelength of visible light limited to approximately 200 nm. As a result it is not possible to see structures below this number. This, however, is a theoretical limit. The microscopes used had a resolution in the μm range. Especially the specimens from the FSR consisted of finer than 200 nm structures and were not observed with this methods.

The microscopes used in this work were stereo- and reflective light microscopes (figure 2.1).

2.2.2 Scanning Electron Microscopy

In scanning electron microscope (SEM), electrons are accelerated towards the sample. The electron beam scans the sample surface and the resulting interaction with the material is registered by sensors. Most widely used for imaging are secondary electrons (SE) and backscattered electrons (BSE) [22].

The SE are emitted by the sample after the beam hits the sample. The origin of the SE is from atoms of the top most nano meters of the sample.

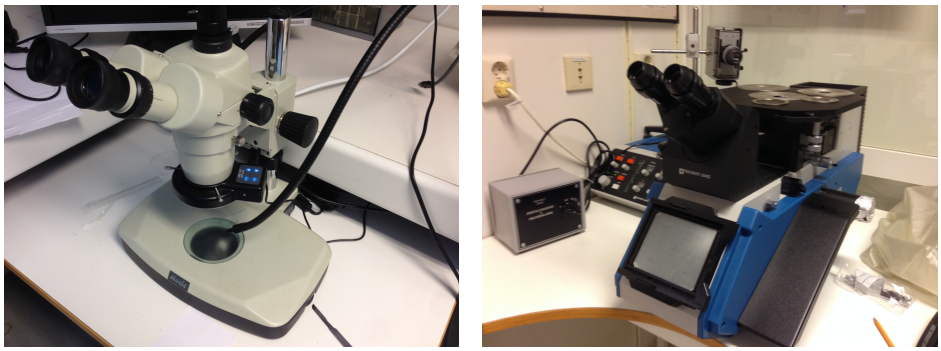

(a) (b)

Figure 2.1: Visible light microscopes used for this work: (a) stereo microscope and (b) reflective light microscope.

(a)

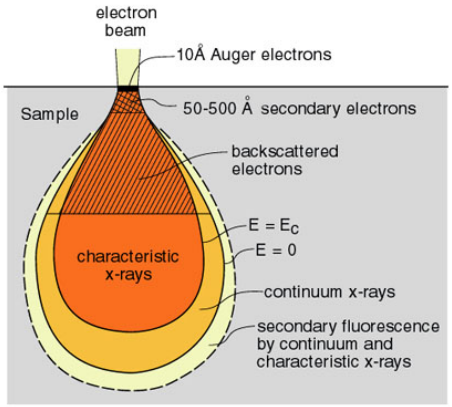

(b)

Figure 2.2: Scanning electron microscope Hitachi TM3000 (a) and (b) schematic image of the penetration depth of electrons into the material (image by [23].

Electrons from deeper atoms do not have the energy to leave the material. The SE have energies of few eV. Since the SE escape solely from the top most layer of the examined material the image taken carries topographic information of the sample.

BSE on the other hand have a significantly higher energy than SE. They are incident electrons that have been scattered at angles close to 180°. Due to the fact that the intensity of the BSE signal is sensitive to the atomic number of the material, the backscattered image shows differences in chemistry of the analysed material. It has to be mentioned, however, that BSE escape quite deep into the material and the measured signals do not only come from the area close to the surface.

2.2.3 Transmission Electron Microscopy

In transmission electron microscopes (TEMs), the detected electrons are transmitted through the sample. Thus the material must be thin enough to be electron transparent. With the use of TEM, even the smallest structures down to the atomic level can be made visible.

It should be noted that with TEM it is assumed that the sample preparation will not alter the microstructure of the sample. Further it is assumed that the very small sampling volume is fully representative of the bulk. Finally, it is assumed that a 2-D slice of this small volume allows us to determine the structure of a 3-D material.

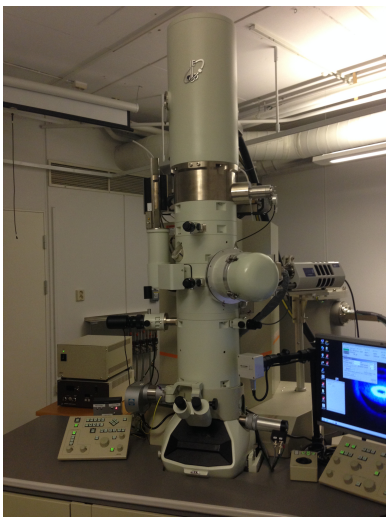

Figure 2.3: Image showing the TEM used for this work.

The used microscope is a Jeol 2100F. The lattice resolution is 0.19 nm at the highest magnification of x=1.500.000. Figure 2.3 shows an image of the TEM that was used in this work.

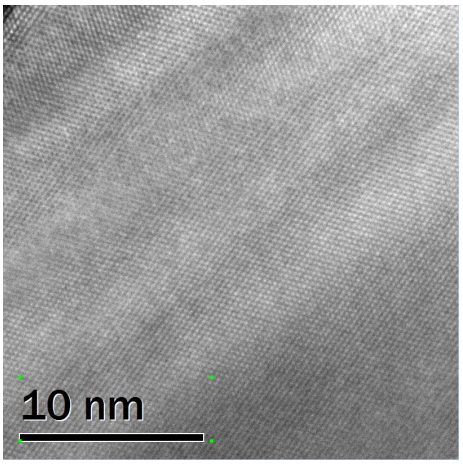

Figure 2.4: HRTEM image of Si in the [111]-zone axis.

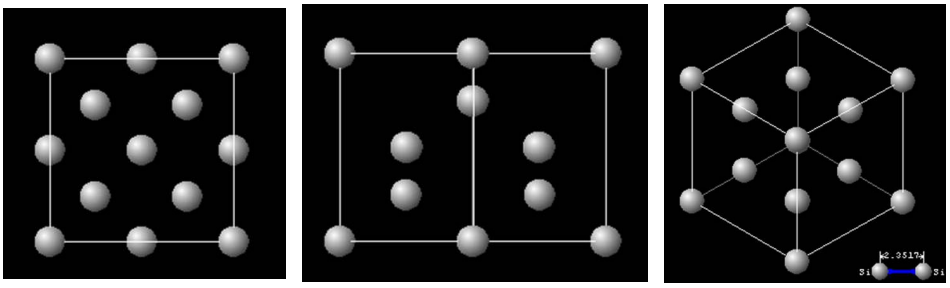

(a) (b) (c)

Figure 2.5: Schematic drawing of three different views on the crystal lattice of silicon with (a) in the <100> direction, (b) the <110> direction and (c) the <111> direction [24].

High Resolution TEM

Silicon has a diamond-type crystal structure, where each atom has 4 nearest neighbours. The unit cell contains 8 atoms and has a lattice constant of 5.431 Å.

With help from the high-resolution transmission electron microscopy (HRTEM), it is possible to see a direct image of the atomic structure of a sample.

A crystal lattice of Si can be seen in figure 2.4. The view is along the [111]-zone axis. A schematic view of three different lattices are given in figure 2.5. There the <100> <110> and <111> directions are presented.

However, more than just single crystals are observable. An overview over three in the context of this thesis relevant structures is given in figure 2.6.

In high resolution TEM defects in the lattice can be seen. Such a defect is e.g. the formation of a twin, where two atom lattices share the same lattice points in a symmetrical manner. This can happen when, in the

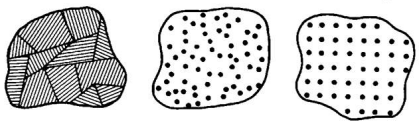

Figure 2.6: A schematic drawing of a polycrystalline (left) an amorphous (middle) and a single crystalline structure.

solidification process, the atoms do not arrange in the perfect manner. Another possibility is introducing the twins by means of mechanical force. Such forces can arise when the material cools. A third way these fault may appear is when particles grow together so that a grain boundary is created.

Electron Diffraction

Electron diffraction is a very effective way to characterize crystal structures. It is characteristic that electrons interact with both the electron cloud and the atomic nuclei of the studied material. They are very sensitive to changes within the lattice such as dislocations or stacking faults. This means that such faults can be surveyed. Just as each material has material specific properties such as the crystal structure, the diffraction has unique characteristics as well.

Two types of scattering are involved in the resulting diffraction pattern (DP): dynamical scattering and kinematic scattering. One very important effect of dynamical scattering is the multiple scattering, where electrons are scattered to otherwise mathematically forbidden reflections.

The second type of scattering is kinematic scattering. Electrons pass through the material and scatter according to Bragg's law:

$$2dsin(\Theta_B) = n\lambda \tag{2.1}$$

where d is the distance between two lattice planes, Θ_B is the angle between incident beam and reflected beam, n is an integer and λ is the wavelength of the electron beam. Figure 2.7 shows schematically scattering according to Bragg's law. It describes that if two incoming rays, after reflecting on the crystal lattice, have a path difference between the rays that is equal to an integer multiple of the wavelength, they interfere constructively. That means that electron waves that are reflected by the materials lattices form a reflection when Bragg's law is satisfied. In this case they form a characteristic pattern.

Figure 2.8 shows such a pattern. It presents a schematic diffraction pattern along three different zone-axes of a silicon crystal: [100], [110] and [111].

2.2.4 X-Ray Diffraction

X-ray diffraction (XRD) is used to determine the structure of a material such as organic or inorganic crystals, down to the molecular and atomic

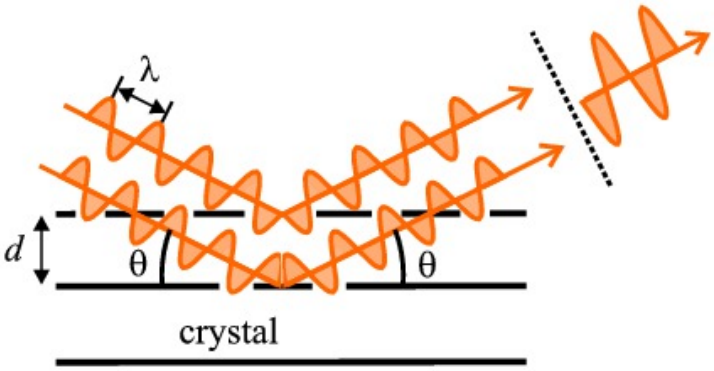

Figure 2.7: Schematic drawing of scattering following Bragg's law [25].

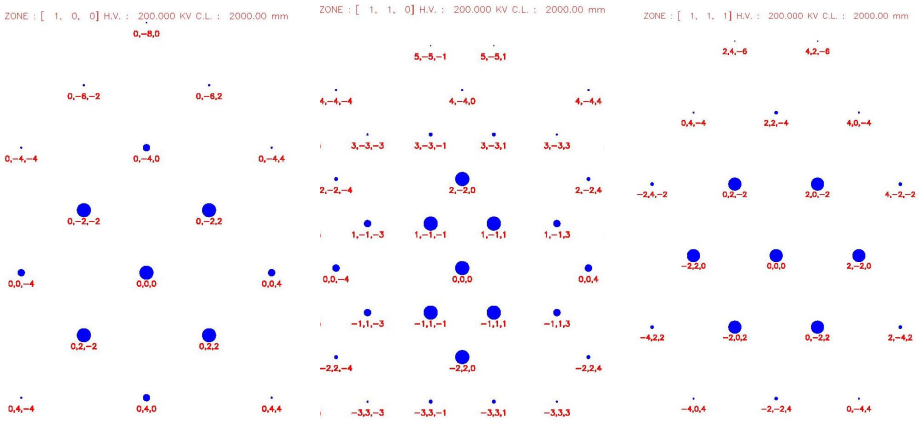

(a) (b) (c)

Figure 2.8: Schematical Selected Area Diffraction (SAD) pattern of silicon: (a) along the [100] zone-axis, (b) along the [110] zone-axis and (c) along the [111] zone-axis [26].

scale. The information gained from XRD is the crystalline phases in their quantitative proportion. It thus gives information about how big of a fraction is crystalline silicon, or other non-amorphous phases such as silicon dioxide (SiO_2) or silicon carbide (SiC). The goal of this experiment is to pinpoint phases such as SiC and get information about how much of non-silicon elements are fixed within these phases. Most important, however, is the information about the crystallinity and also the crystallite size of the analysed material.

$$t = \frac{0.9\lambda}{Bcos\theta_B} \tag{2.2}$$

The size of the crystallites were calculated using Scherrer formula in equation 2.2, where t is the average thickness of the crystallite, λ is the wavelength, in this case of the X-Ray source, B is the broadening at the root of the peak, and θ_B is the Bragg angle [27].

The instrument used for the experiments was a Bruker-Siemens D8 Advanced diffractometer with a Cu-Kα radiation source.

2.2.5 Calculation of porosity

In order to determine the porosity of a material, grayscale images from polished samples taken with the reflective light microscope have been used. With help from the image analysing software ImageJ the grayscale images were loaded and transformed into binary images. Since the metallic material was ground and polished, the surface was mirror-like. Thus, when transforming into binary images the metal becomes white and the voids black. The histogram now shows the amount of white and black pixels. By dividing the amount of black pixels with the total amount of pixels results in the fraction of voids in the material.

3. Results

In this project, silicon samples have been analysed and characterised with different tools. This chapter shows the results obtained using the particular methods.

3.1 Free Space Reactor

Specimens from the FSR show great similarities in terms of structure, specifically in low magnifications. Thus there were no pictures captured using VLM. For the same reason, the fine structure, SEM images were not giving significant information to differentiate the samples from each other. Nonetheless one set of images is presented to show an overview of the powder specimens. Figure 3.1 shows images from sample Fi575 in different magnifications. They are representative for all samples from the Free Space Reactor. The powder is, as the images show, very homogeneous, containing small particles with a average size of under one μm. As these are powders, the distribution is entirely random. It can also be said that the particles are too small to see their finest features with the microscope used.

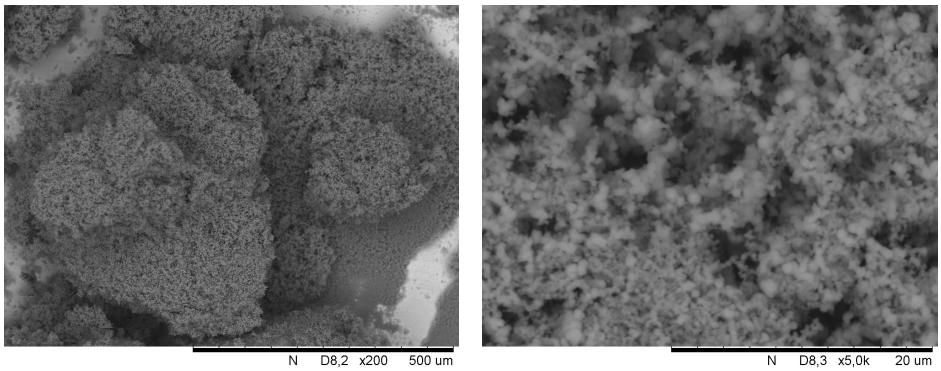

(a) (b)

Figure 3.1: SEM images of sample Fi575 at two different magnifications.

3.1.1 Sample Fi600

The powder from sample Fi600 consist of both crystalline and amorphous particles. The particle size of this specimen ranges from about 50

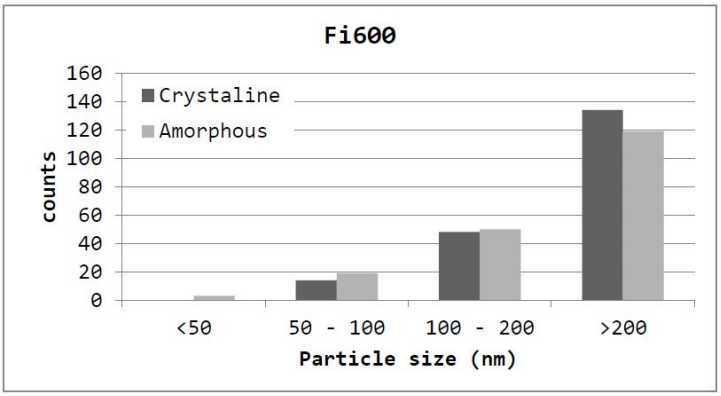

Figure 3.2: Plot showing the size distribution of the crystalline and amorphous particles from Sample Fi600.

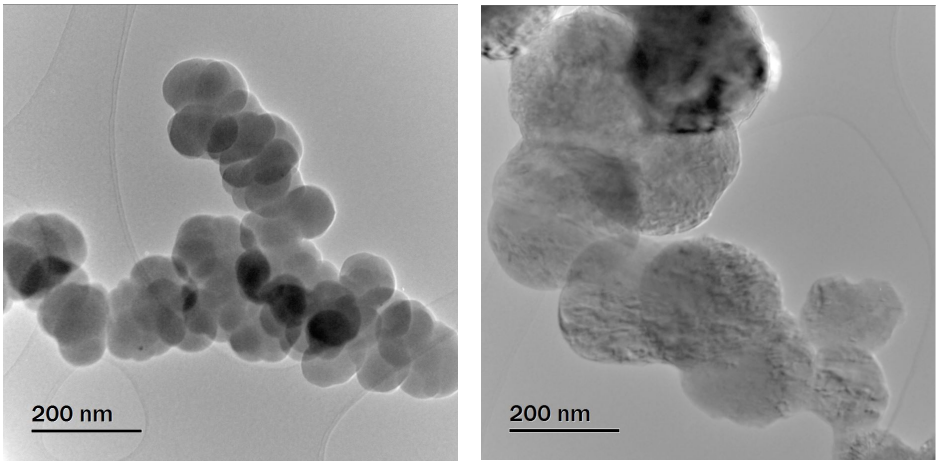

(a) (b)

Figure 3.3: TEM image of sample Fi600 with an amorphous (a) and a crystalline (b) agglomerate part.

nm to several 100 nm diameter of the spheres. Figure 3.2 shows the size distribution of particles separately for crystalline and amorphous agglomerates. It shows that the fraction of amorphous and crystalline particles throughout the particle size is close to equal. It can also be seen that most particles are larger than 200 nm.

In all observed cases the particles grew together to form agglomerates. There is no mixture between amorphous and crystalline particles in the agglomerates. That means that the whole agglomerate is either crystalline or amorphous. The individual particles are spherical, the agglomerates appear to be chains of round particles. Figure 3.3 shows such agglomerates. High resolution images and diffraction patterns show that the crystalline spheres do not consist of single crystals. Figure 3.4 visualises a sphere in high resolution and the diffraction patter of that area.

The size differences in figure 3.3 a and b are not representative for the

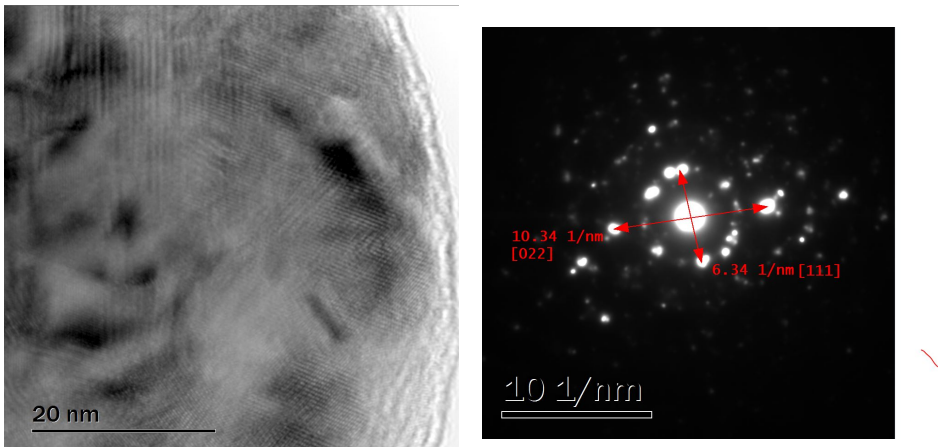

(a) (b)

Figure 3.4: HRTEM and diffraction images of crystalline sample Fi600.

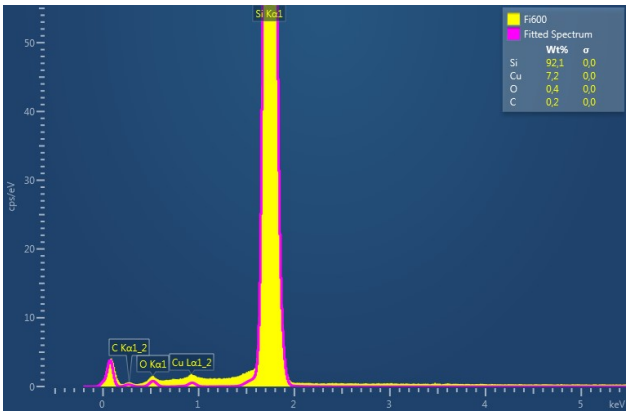

Figure 3.5: EDS plot from sample Fi600.

whole material as described before. The visual difference between amorphous and crystalline particles is the contrast. While in the amorphous agglomerate each particle is very homogeneous in it self, they can be distinguished with thickness and mass contrast. The crystalline particles, however, show a contrast within each particle due to diffraction contrast. This difference is very well displayed in figure 3.3. Due to this difference the amorphous particles appear smoother and rounder, where the crystalline particles in contrast seem to be less perfect shaped with bumps and dents.

The high resolution image in figure 3.4 shows an inhomogeneous lattice structure where it looks like many different orientations are grown together. The diffraction pattern in 3.4b from the same yet bigger region shows reflections from many crystals, so it can be assumed that the crystalline particles analysed are in fact nanocrystalline.

Figure 3.5 shows the result of an EDS measurement of particles from sample Fi600 in TEM. Clearly visible is the biggest peak belonging to silicon. The smaller peaks from Copper (Cu) and Carbon (C) carbon

come from the sample holder,which originates from the holey carbon grid. Oxygen (O) originates from the apparently oxidized surface of the Si-powder.

3.1.2 Sample Fi575

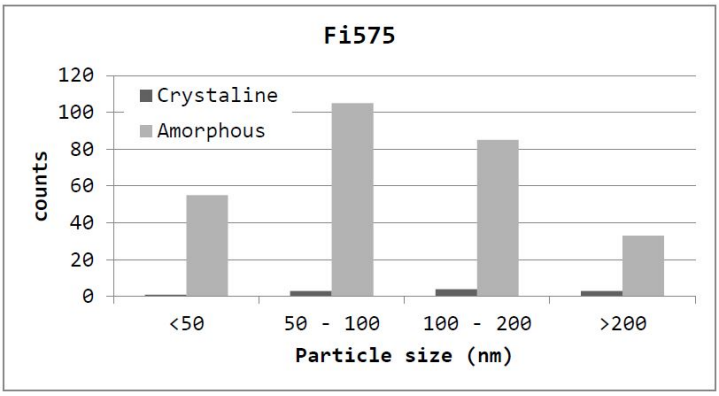

Figure 3.6: Plot with counted amorphous and crystalline agglomerates from sample Fi575.

This sample shows just as Fi600 a great variety in particle size ranging from below 50 up to more than 200 nm. Figure 3.6 shows the distribution of particle size of the crystalline and amorphous agglomerates. In this plot it becomes apparent that there are almost no crystalline particles. However, the distribution of the amorphous particles indicated that most of the spheres are between 50 and 100 nm in size.

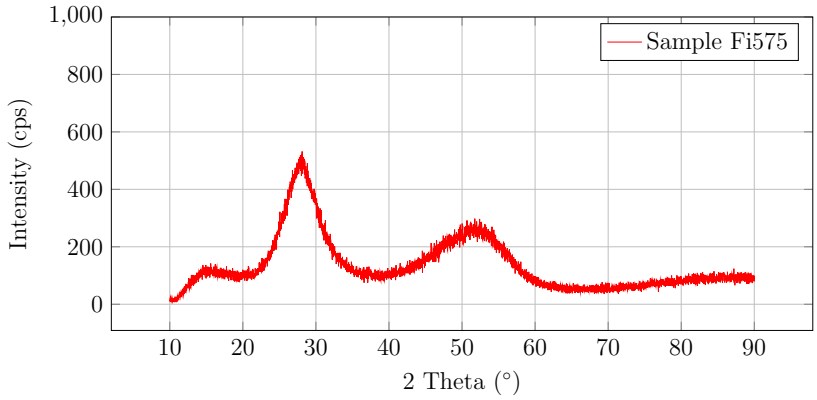

Figure 3.7: XRD graph from sample Fi575.

In figure 3.7 the results from the XRD experiment from sample Fi575 are shown. The graph appears to be wave-like. Since there are no sharp peaks in the plot it can be assumed the powder tested is free or mostly free of big crystalline particles. The first significant bump peaks around 28° which is similar to the (111) peak of crystalline silicon. The second bump is

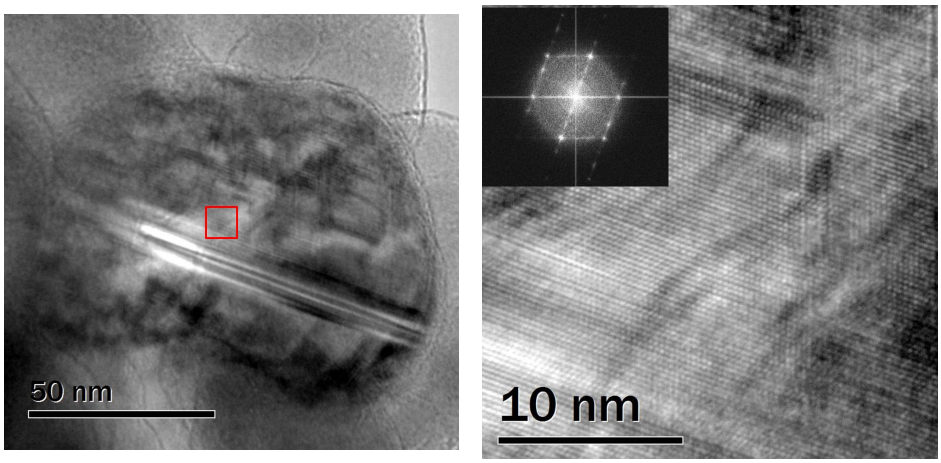

(a) (b)

Figure 3.8: TEM image of a crystalline particle (a) and the HRTEM image from the marked area of sample Fi575. The FFT image in the corner of image (b) is from the marked area.

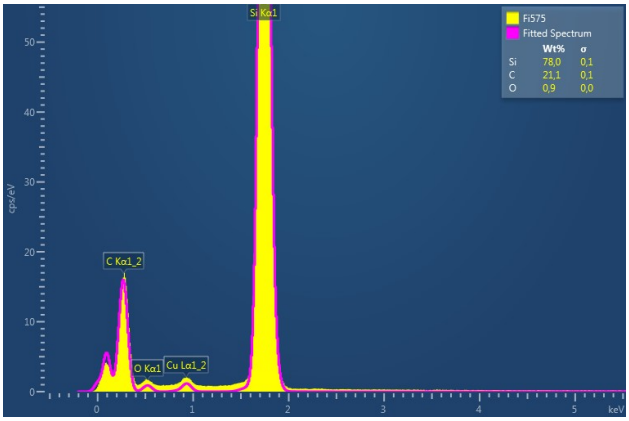

Figure 3.9: EDS plot from sample Fi575.

approximately at 52° and thus between the (220) and the (311) peak of the crystalline sample.

Figure 3.8 Shows a crystalline particle from sample Fi575. It appears that the particle is surrounded by amorphous particles. In the relative low magnification (a) it is already visible that the crystal contains stacking failures. In the high resolution image (b) the stacking errors become visible. The FFT image in the corner of (b) is from the area of (b). It shows a tripling in the pattern.

The Results from the EDS measurements in figure 3.9 show a high silicon content. Elements such as copper, carbon or oxygen are measured because of the sample holder and the exposure of the specimen to air. Thus it can be assumed that the sample powder is pure silicon.

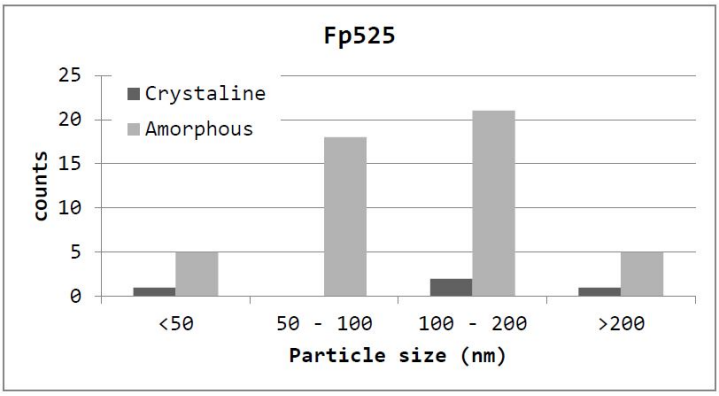

Figure 3.10: Plot with counted agglomerates from sample Fp525.

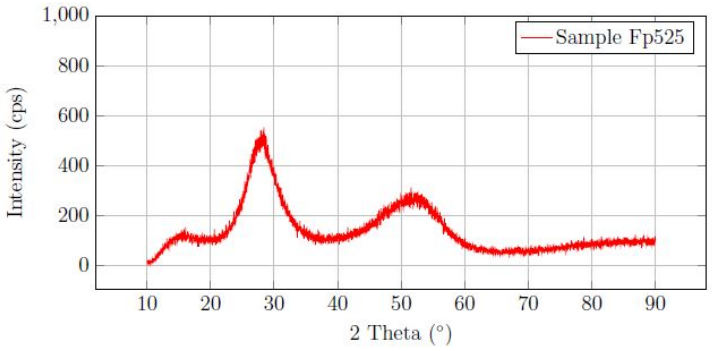

Figure 3.11: Graph from the XRD experiment showing the result for sample Fp525.

3.1.3 Sample Fp525

Sample Fp525 as well shows both crystalline and amorphous particles. However, as figure 3.10 shows the amorphous agglomerates are much more numerous. Most frequent are particles in the size range from 100 to 200 nm and slightly less frequent are those with size from 50 to 100 nm.

The results from the XRD experiments are shown in figure 3.11. The plot shows large bumps at about 28° and 52°. The position of the bumps is on the same position as the ones from sample Fi600. A calculation in order to determine the crystallite size of that material resulted in an average size of 16 Å.

Figure 3.12 shows an example of a crystalline particle and its corresponding diffraction pattern. This sphere shows the same crystal orientation throughout the material. However, lattice imperfections are visible. The imperfections within the particle appear to be in the directions of the lattices. As can be seen from the SAD pattern in figure 3.12b there are extra reflections in the <111> direction of Si.

Image 3.13a is an overview of several crystalline spheres. In this image it appears that two spheres grew together. A detail of this figure is visible in image 3.13b. It can be see in this figure, that there is no apparent

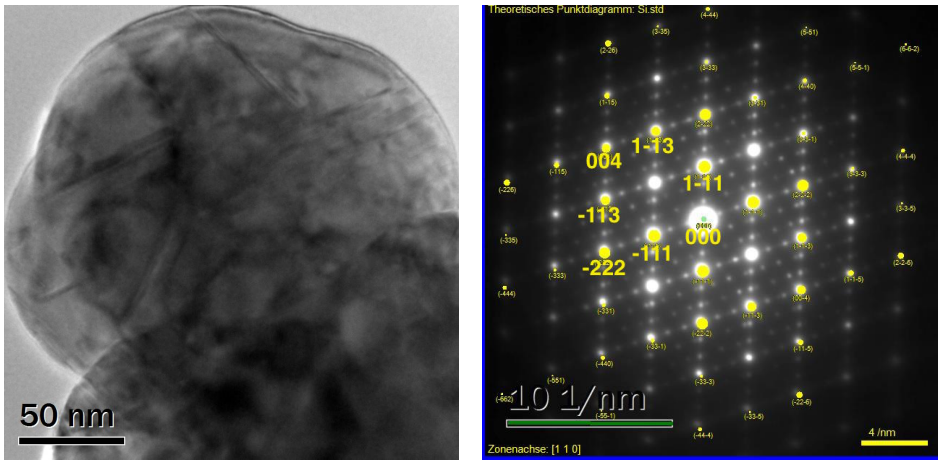

(a) (b)

Figure 3.12: TEM- and diffraction image of a particle of sample Fp525.

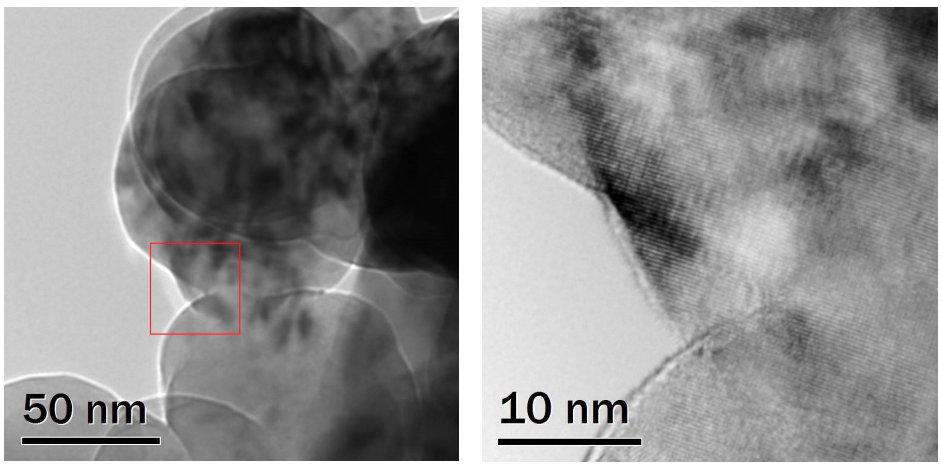

(a) (b)

Figure 3.13: High resolution images of sample Fp525 showing several particles grown together (a) and the boundary-free transition from one particles to another (b).

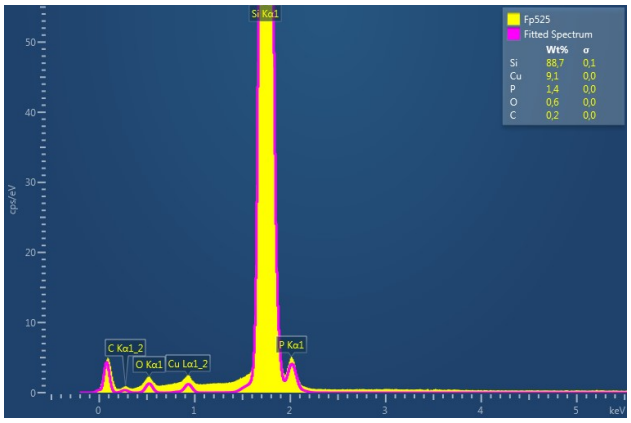

Figure 3.14: EDS plot from sample Fp525.

grain boundary between the two particles. It is also visible, that the lattice direction is not changing from one sphere to the next.

The results of the EDS measurements from sample Fp525 are shown in figure 3.14. In this plot the elements expected due to the sample holder and oxidation of the sample powder are present. These are Cu, C and O. The percentage of Si according to the measurement is 88.7 wt.% and one of the doping element P is 1.4 wt.%. However, adding the 9.9 wt.% from Cu, C and O gives approx 1.5 wt.% P and thus 98.5 wt.% Si, assuming that none of the contamination elements are present in the powder.

3.1.4 Sample Fp575a

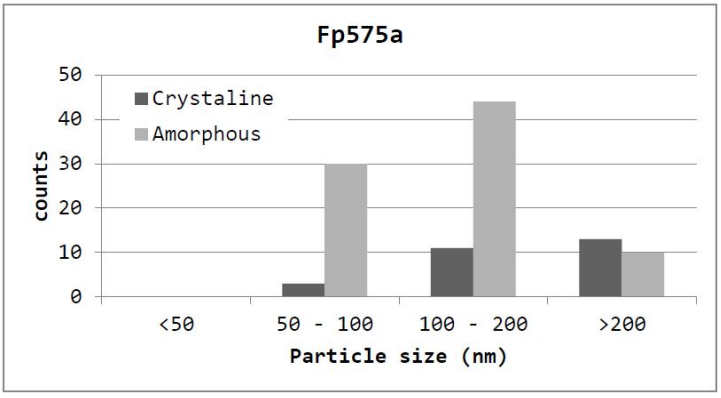

Figure 3.15: Plot showing the particle size distribution of amorphous and crystalline particles from sample Fp575a.

The particle distribution shown in figure 3.15 shows a significantly higher amount of amorphous particles. No particles in size smaller than 50 nm were observed. The much more abundant amorphous particles have the highest count in the size range 100 to 200 nm followed by 50 to 100 nm. The counted crystalline particles on the other hand have the highest count in the range bigger than 200 nm.

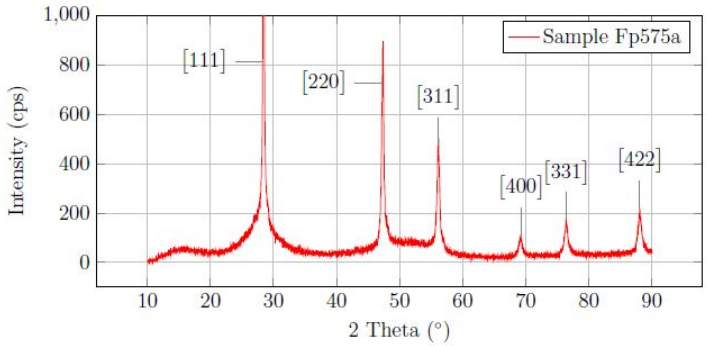

Figure 3.16: XRD analysis of sample Fp575a.

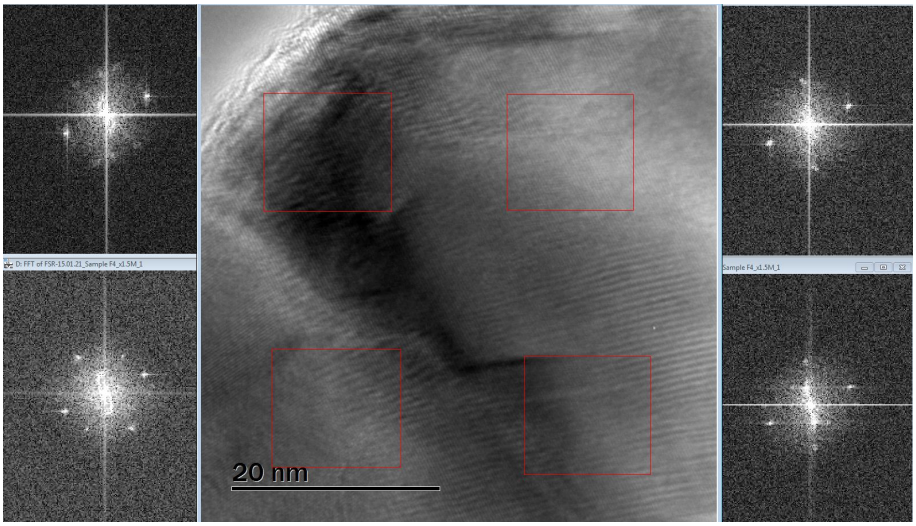

Figure 3.17: TEM image of sample Fp575a with four Fourier transformations from small areas as marked in the image.

The XRD graph from sample Fp575a in figure 3.16 shows crystalline particles in the tested sample. The clearly visible peaks are indicated and appropriate for silicon. The broadening at the bottom of the peaks points the amount of amorphous particles.

Figure 3.17 shows a high resolution image of a sphere from sample Fp575a. In the figure the lattice structure is visible. The four FFT images right and left of the HRTEM image are from the indicated areas (red squares). In the TEM image it is visible that the lattice orientations are changing throughout the whole particle. The FFT images show, that even on the small area of the analysed particle, the changes are significant.

In the EDS plot seen in figure 3.18 a very similar image compared to the previous one can be found. The elements Cu, O and C are present, as they are from the environment of the powder. Removing these elements from the calculation results in an approximate P content of 1.1 wt.% and 98.9 wt.% Si.

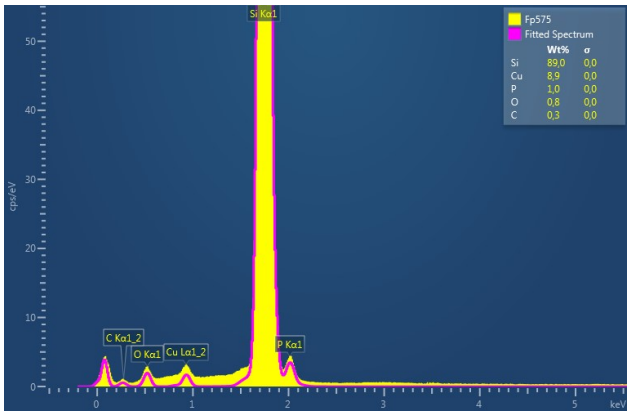

Figure 3.18: EDS plot from sample Fp575a.

3.1.5 Sample Fp575b

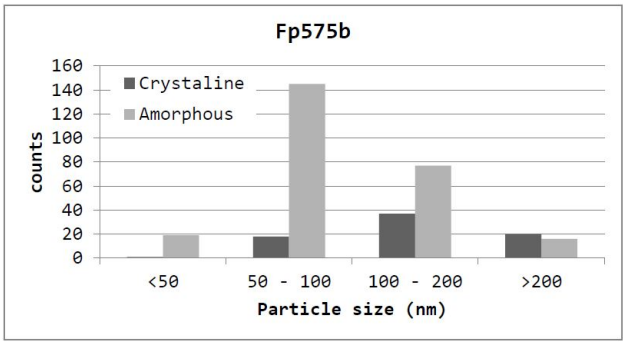

Figure 3.19: Plot with the counted crystalline and amorphous agglomerates with respect to their particle size.

In figure 3.19 the particle size is plotted against the number of counted agglomerates. The amount of amorphous particles is significantly higher, the highest number of those spheres lies in the size range from 50 to 100 nm.

The XRD graph in figure 3.20 shows three well visible peaks. They are at the same position as in the previous sample and characteristic for silicon. The plot is very flat due to the little count time. This also reduced the height of the peaks. All visible peaks are indicated appropriately.

Figure 3.21 shows SAD image of sample Fp575b. It can be seen in the image that both amorphous and crystalline particles are present. The rings created by the amorphous and polycrystalline material are well distinguishable and indicated appropriately.

This sample shows no ground-breaking differences compared to the previous ones. Here, as well, both crystalline and amorphous particles have been observed. In image 3.22a a crystalline particle surrounded by amorphous particles can be seen. The high resolution image of that particle, image 3.22b, shows the lattice. The blurriness is due to amorphous particles

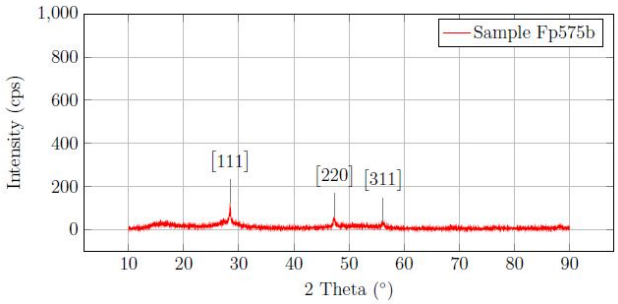

Figure 3.20: XRD graph with the results from sample Fp575b.

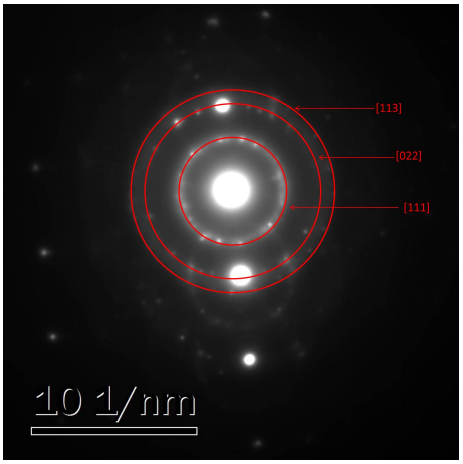

Figure 3.21: SAD image of crystalline and amorphous particles from sample Fp575b.

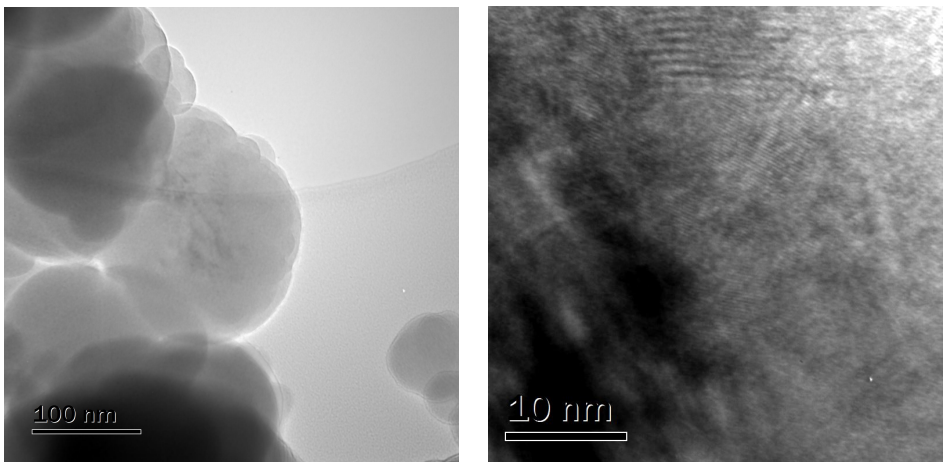

(a) (b)

Figure 3.22: TEM image of sample Fp575b with an agglomerate (a) and the higher resolution of crystalline (b) and amorphous (c) particles.

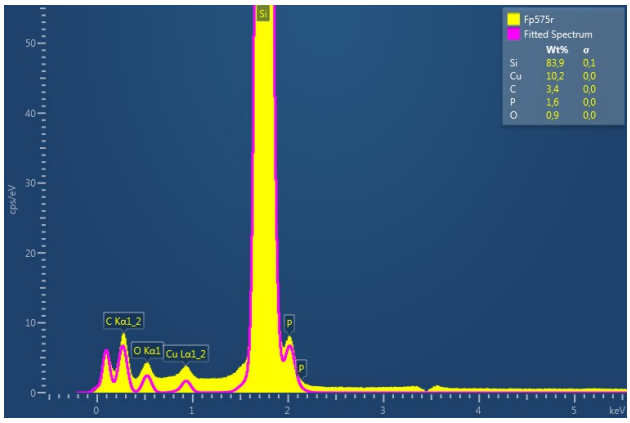

Figure 3.23: EDS plot from sample Fp575b.

underneath the crystalline.

The EDS measurement from the TEM shows silicon and phosphorous in the sample material. It is assumed that the other elements measured are due to surroundings and the samples exposure to air.

3.2 Dynatec Centrifuge Reactor

Two sets of samples from the Dynatec Centrifuge Reactor have been investigated.

3.2.1 Sample Di

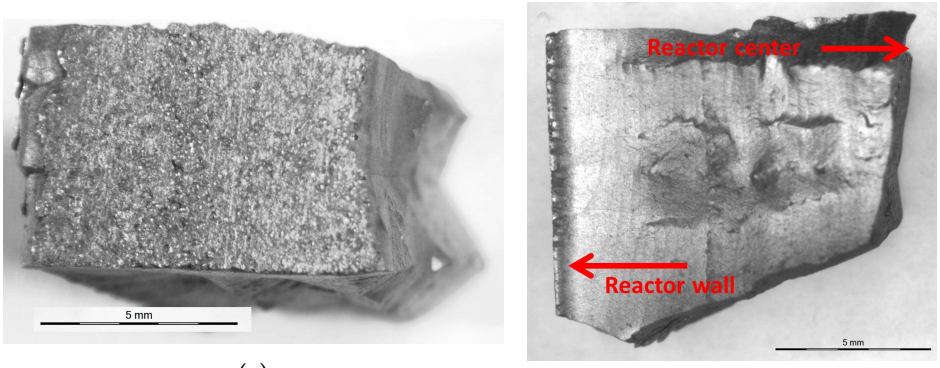

(a) (b)

Figure 3.24: Stereo microscopic image of sample Di-w-a with: (a) showing the side facing towards the reactor wall and (b) the cross section.

Sample Di originated from 3 regions of the Dynatec reactor: the top of the reactor wall (Di-w-a), the ceiling (Di-r) and the exhaust (Di-ex). The sample from the reactor wall appears to have grown into a dense crystal. As it can be seen in image 3.24a, the surface towards the reactor wall is

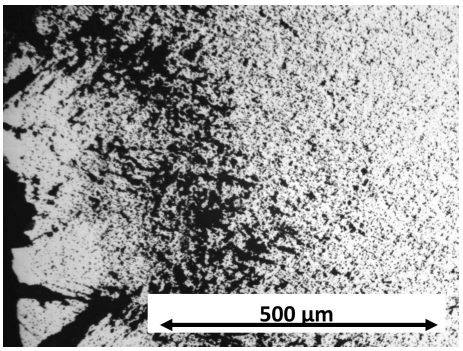

Figure 3.25: Reflective light image of sample Di-w-a from a site close to the wall. The red bars indicate the V-shaped growth direction from the seed particles.

rough and appears inhomogeneous. In image 3.24b it is visible that the side towards the reactor contains grains, which were inserted before the CVD process started. These particles can be seen in the side facing the wall. The growth of the crystals looks homogeneous throughout the whole length. The total thickness of the grown material, i.e. the length of the crystal, is approximately 12 mm.

The particles on the wall side of the sample are clearly visible in the ground and polished material as well as it can be seen in figure 3.25. It is mentionable that the particles have a very low porosity compared to the rest of the crystal. In particular the area around the particles show a very hight porosity, the interconnection between the particles appears to be little. The material grows, starting from the seeds, all more or less in a V-shape, as indicated in figure 3.25. The consequence is that some overgrow others. After a few hundreds of μm an even layer of very porous material is built up. This layer changes into a rather homogeneous material with significantly fewer voids. The porosity of the seed particles was between 6.6 % and 10.7 % while approximately 36 % of the material between the particles were voids.

In SEM the seed particles are very well seen as well. In figure 3.26, it is very well visible that the seeds are largely free of pores. Directly beside them, however, big voids can be observed. The V-shaped growth originating from the seed particles is very well visible.

Figure 3.27 shows two regions from sample Di-w-a. The different porosities are evident in image 3.27a, which is taken from the edge towards the reactor wall. Image 3.27b is approximately from the middle of the crystal. It can be seen that there are some big voids in the bulk material. It appears that the growth process was interrupted in these regions. New material growth started again and the V-shape as they were mentioned from the seed particles. The porosity measured in the bulk region was between 12 and 16.4 %. Within the bulk material some big voids can be seen. The growth process of the material seems to be interrupted, followed by a new starting point including the pursuing V-shape.

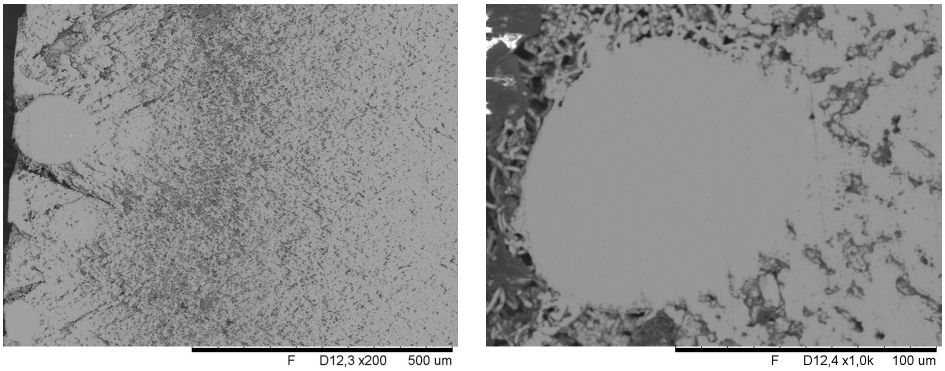

(a) (b)

Figure 3.26: SEM image of sample Di-w-a magnifying areas from the edge of the specimen (near the wall).

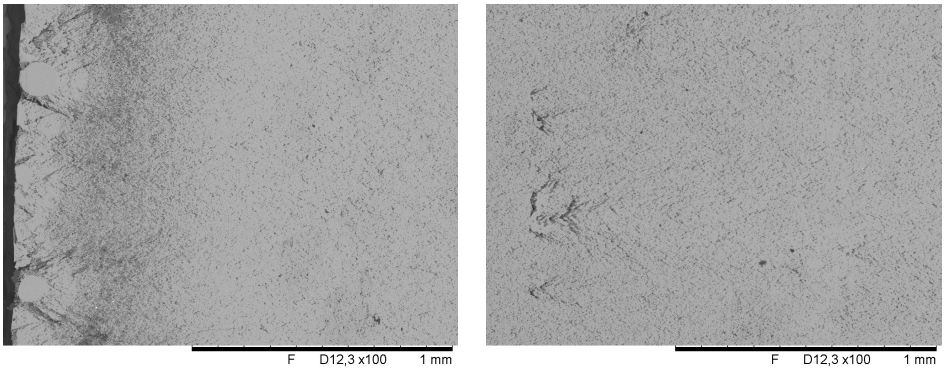

(a) (b)

Figure 3.27: SEM image overview of sample Di-w-a: (a) at the edge to the reactor wall and (b) approximately from the middle of the crystal.

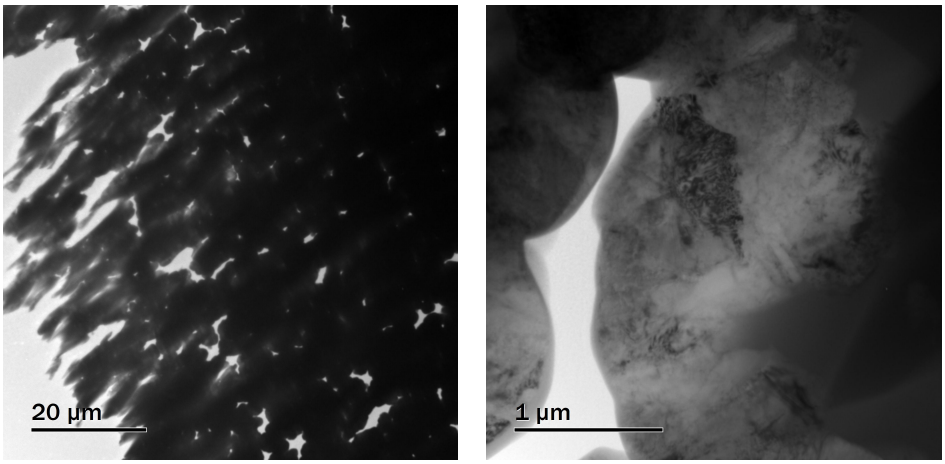

(a) (b)

Figure 3.28: TEM image with an overview of sample Di-w-a showing the structure in low magnification mode (a) and a close up of one sphere (b).

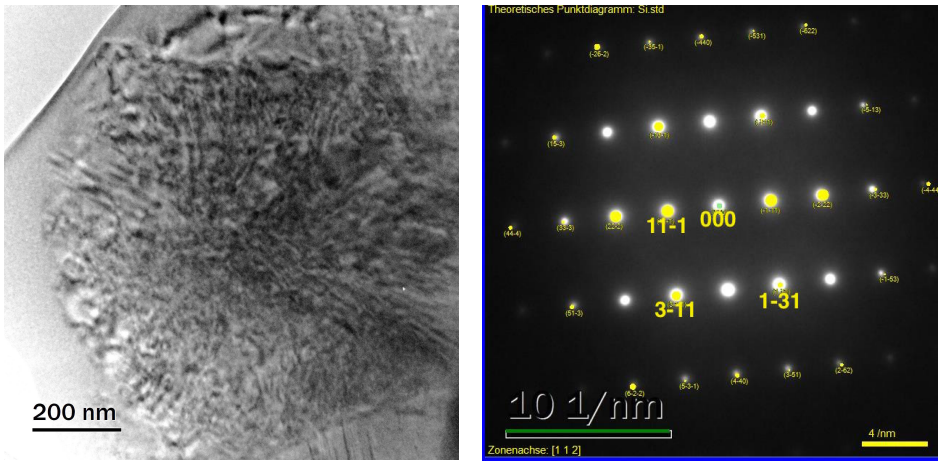

(a) (b)

Figure 3.29: Detail TEM image of a crystalline sphere from sample Di-w-a (a) and the appropriate diffraction pattern (b).

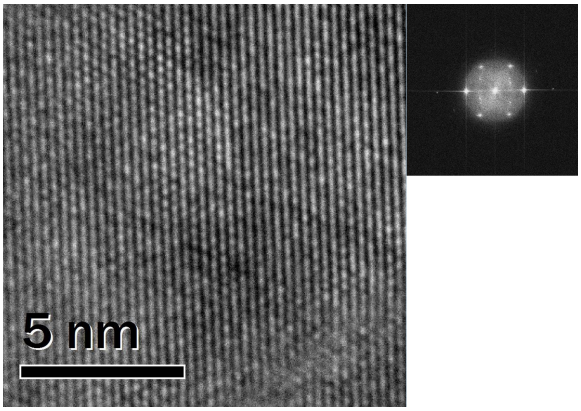

Figure 3.30: The lattice structure of sample Di-w-a and the appropriate FFT image.

TEM show a crystalline material throughout the sample. As the images of figure 3.28 show the material is full of voids. The elongated crystal shape to the left of image 3.28a are due to the ion-milling process. At higher magnification (figure 3.28b) it becomes evident that the material is built up of spheres that have grown together.

High resolution images of this material is shown in figure 3.29a. It shows crystalline micro structure throughout the whole material. At the edges however an amorphous layer is visible originating from the ion-milling during the sample preparation. Figure 3.29 gives a representative image of the micro structure of sample Di-w-a. It appears that the presented sphere is a single crystal material, the appropriate diffraction pattern of the presented sphere is shown in figure 3.29b.

In figure 3.30 the crystal structure of sample Di-w-a can be seen. The lattice appears without disturbances and twins. The lattice structure and

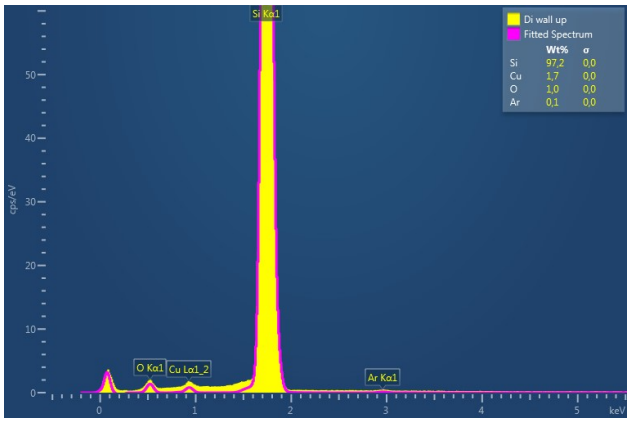

Figure 3.31: EDS plot from sample Di-w-a.

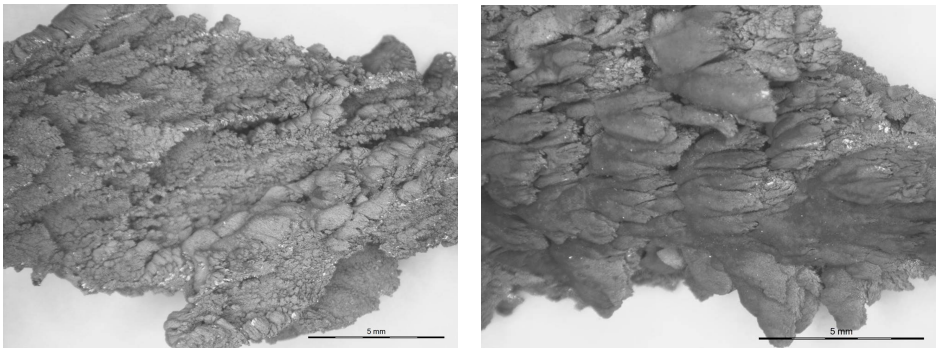

(a) (b)

Figure 3.32: Stereo microscopic image of sample Di-r with: (a) view on site of fracture from loosening the specimen from the reactor roof and (b) view from reactor centre.

the FFT suggest a view from the <111>-direction.

The EDS analysis of sample Di-w-a shows an almost pure silicon sample. However, the other elements, copper, oxygen and argon, are assumed not to be from the original sample. Copper is believed to originate from the ring, where the sample is glued on, oxygen is due to the oxidation of the sample on air and argon comes from the ion milling as the last step of the sample preparation process. Removing these elements leaves a pure silicon specimen.

The density of sample Di-r is significantly different than sample Di-w-a. The material is very light and porous, it has to be handled with care in order not to break it. From the light microscope image in figure 3.32 it can be seen that the material has a chaotic structure and high porosity. The inhomogeneous matter seems to be solidified without apparent order. It has a somewhat sponge-like look. The fracture surface seen in figure 3.32a is rougher and with sharp edges. Figure 3.32b on the other hand has a fine layer of powder on top. The form looks as if it was shaped by gas flow. The shapes are smooth and only few sharp edges can be seen.

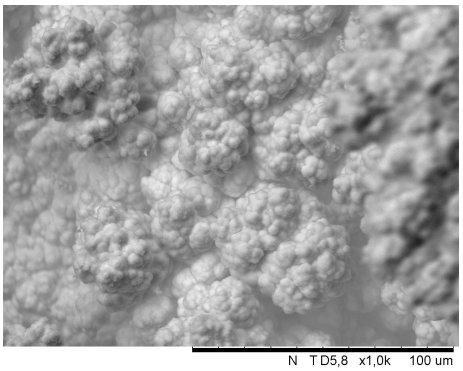

Figure 3.33: SEM image of sample Di-r from the fracture site.

Due to the structure neither sample Di-r nor Di-ex have been studied with the reflective light microscope

The SEM images of the fractured side from this sample, figure 3.33, shows in more detail the surface of the material. The material appears as if it consist of many bubbles, only a few μm in size, that stick together and form a bigger unit. These units again stick together with other units to form even bigger shapes 50 and more μm in size, the particles are not densely packed. At this magnification there is nothing of its previous mentioned sharp edges visible. Nonetheless there is no particular growth direction visible, just that the particles are packed on top of each other.

The surface towards the reactor centre shows smoother features, although a surface roughness is clearly visible (figure 3.34a and 3.34b). The image suggests that a dominant flow direction existed.

Higher magnifications shows that also on the surface towards the gaseous phase the material looks as if spheres grew together as it can be observed in figure 3.34. The surface roughness and topography differs from the fractured side slightly, on the side towards the reactor centre the particles appear to be tighter packed. A close look at image 3.34c shows powder particles of the surface. The particles are in the sub-μm range and appear to be agglomerated together.

Sample Di-r was ground and made into a thin slurry using ethanol. A drop of this slurry was given onto a holey carbon grid and dried. As it can be seen in image 3.35a, two different kind of particle can easily be distinguished. Firstly there are relatively big particles, up to several μm in diameter, bright grey particles with sharp straight edges and appear to be transparent. Secondly, small, dark particles stick together to form agglomerates.

High resolution TEM images of the particles reveals that the structure is significantly different. High resolution imaging and diffraction of chosen areas of each kind of particle shows that the big and rather transparent parts are amorphous, whereas the much smaller and darker particles are obviously crystalline. Figure 3.36 shows both high resolution and diffraction images of sample Di-r. The diffraction patterns are from the

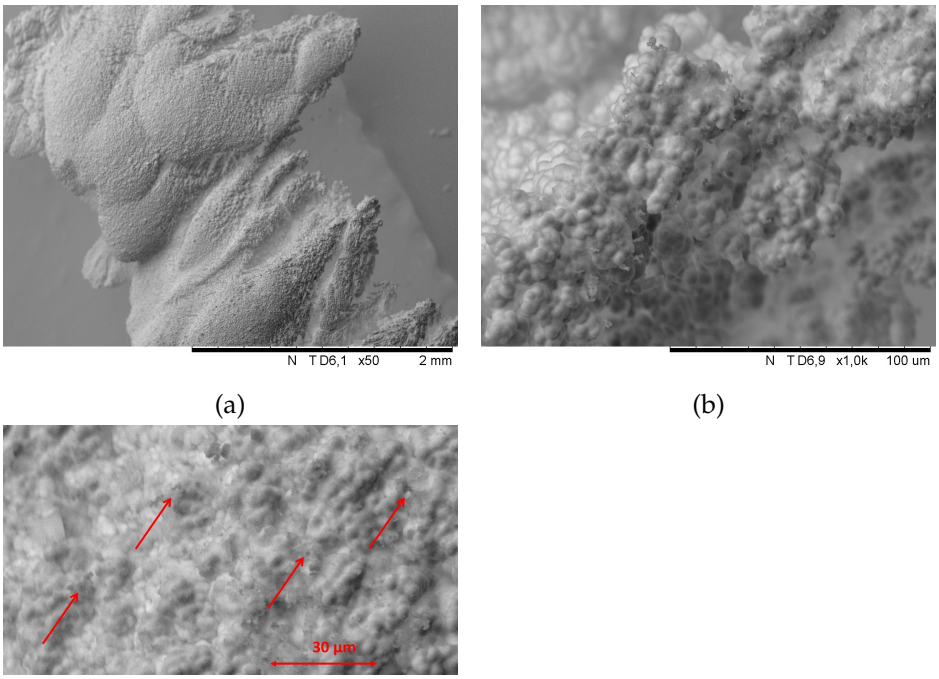

(a) (b)

(c)

Figure 3.34: SEM images of sample Di-r from the surface towards the reactor centre. (a) shows an overview where the structure due to gas flow is visible, (b) is a higher magnification of that area and (c) pointing out the dust particles on the surface.

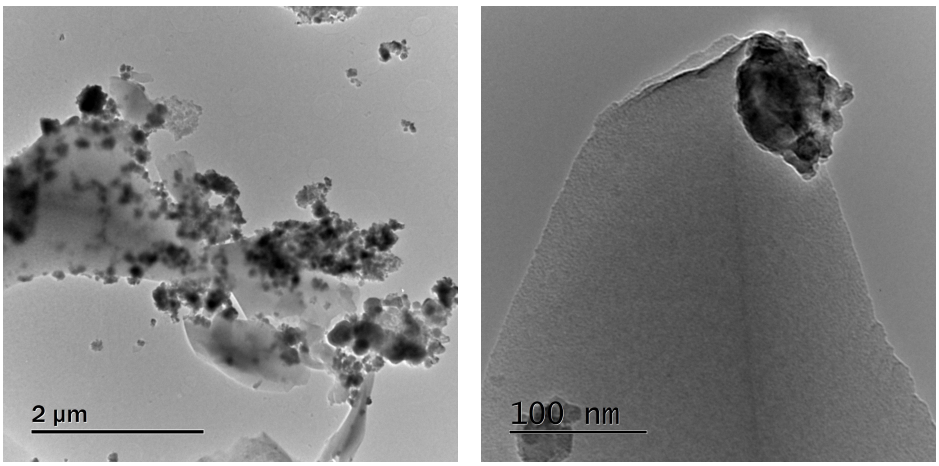

(a) (b)

Figure 3.35: TEM image with an overview of sample Di-r

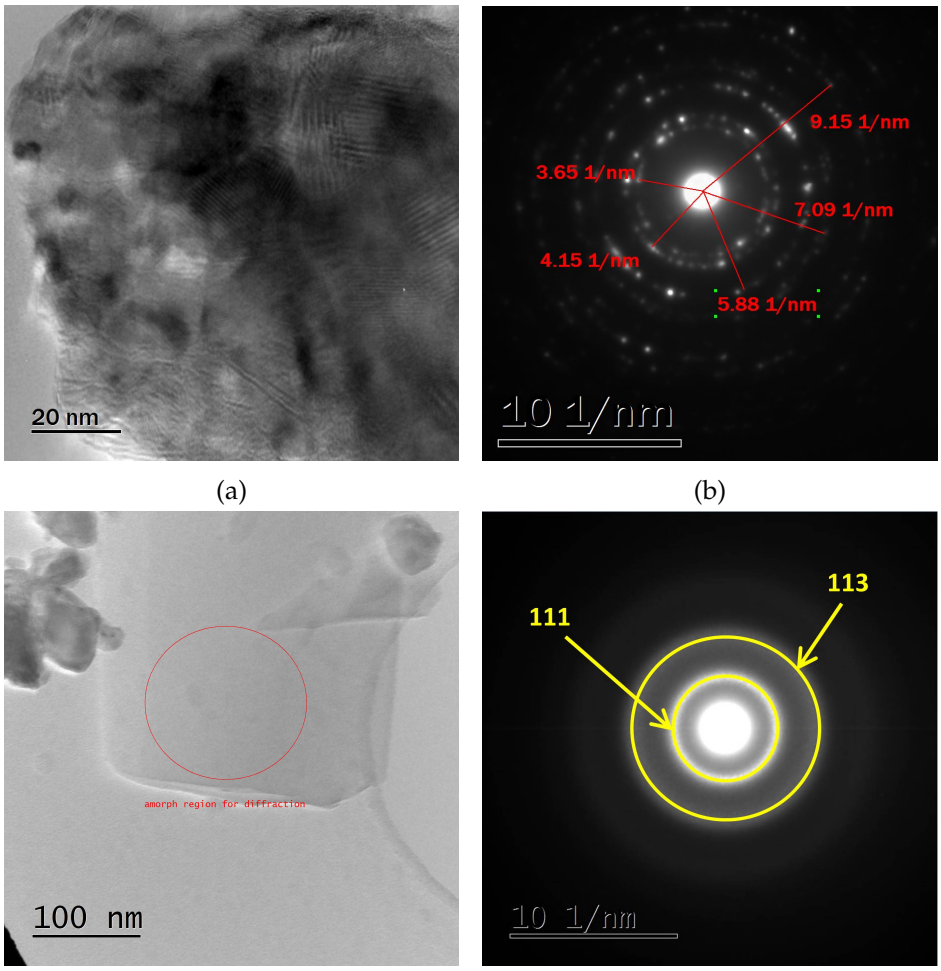

(a) (b)

(c) (d)

Figure 3.36: HRTEM and diffraction images of crystalline (a + b) and amorphous (c + d) particles of sample Di-r.

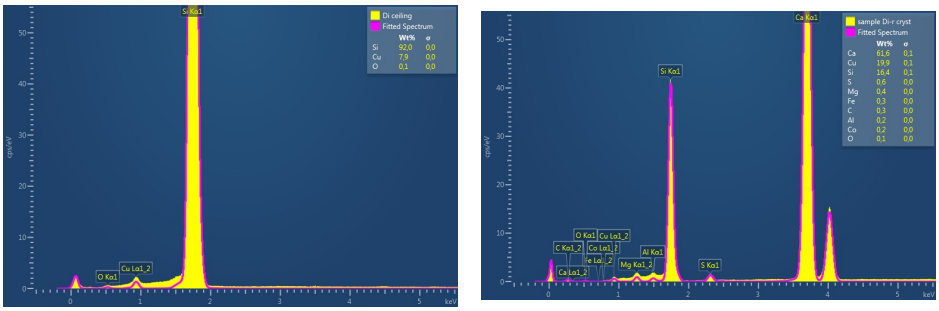

(a) (b)

Figure 3.37: EDS spectra from sample Di-r showing the composition of (a) an amorphous particle and (b) a cluster of crystalline particles

Figure 3.38: Stereo microscopic image of sample Di-ex

noted areas in the HR images. Image 3.36b shows the diffraction pattern of a polycrystalline material. The area where the diffraction pattern was taken from is marked in the TEM image 3.36a. Image 3.36c shows the amorphous crystal with the marked area for the diffraction.

The result of the EDS analysis for amorphous particles from sample Di-r is shown in image 3.37a. It can be seen the amorphous particles are largely pure Si. Only the elements that are assumed to come from the environment, O and Cu, are present as well. Image 3.37b shows the measurement from a crystalline area.

The last specimen taken out of the batch from sample Di was a powder caught by the exhaust (3.38). The shapes that look like grains appear to have agglomerated together to become larger particles. However, if touched, these grains fall apart immediately into fine powder. No other special features were noticed using visible light microscopes.

In SEM, however, it shows that these particles melt together and the borders between them become indistinct (figure 3.39). In the highest magnification (figure 3.39b) it is visible that these are in fact not big particles but rather collections of fine powders sticking together.

In TEM it has been found that the greatest amount of the particles are amorphous. However, there were very few crystalline particles. In fact only one agglomerate containing non-amorphous silicon was observed.

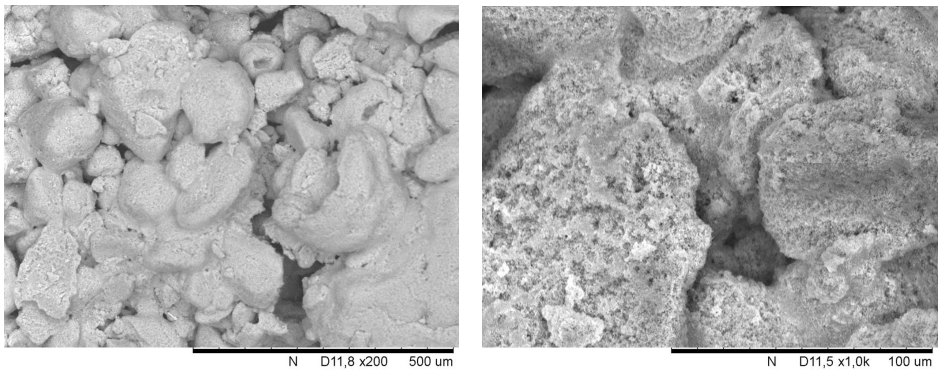

(a) (b)

Figure 3.39: SEM images of sample Di-ex showing in two magnifications the structure of the grains of the sample powder, reviling that it, in fact, consist of much finer particles that it can be seen in VLM.

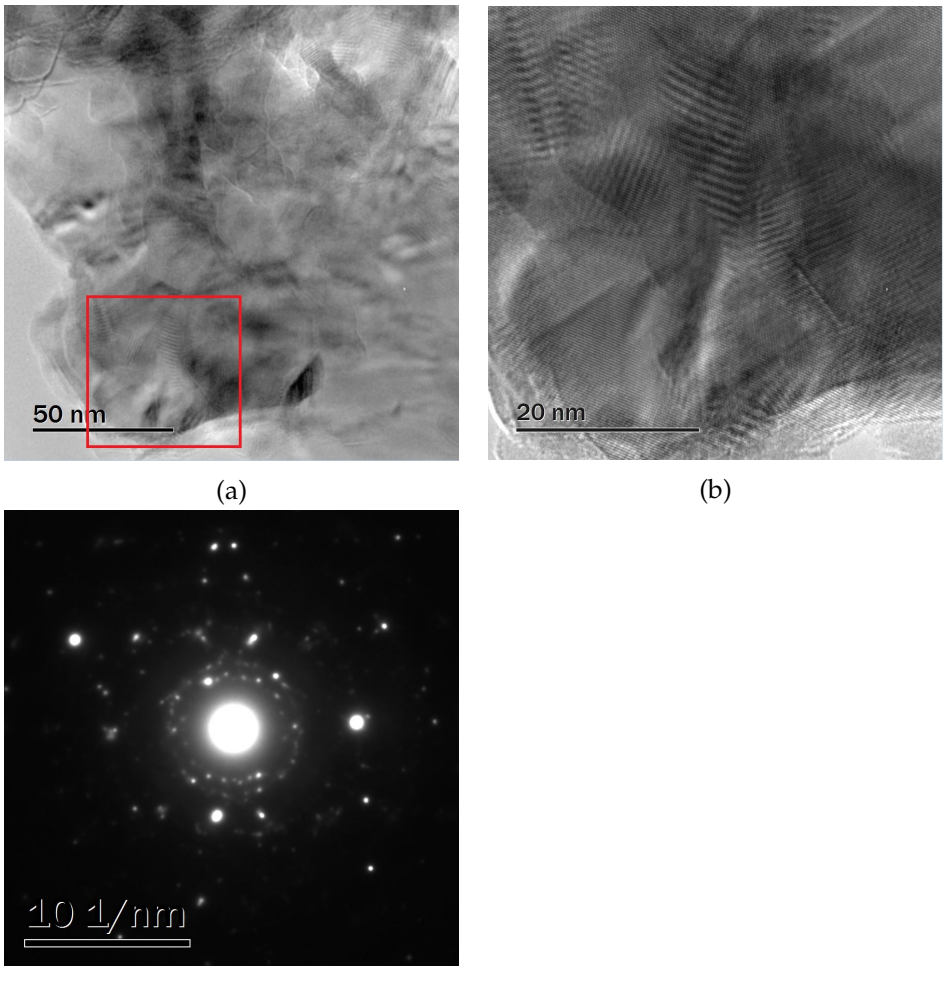

(a) (b)

(c)

Figure 3.40: TEM image showing polycrystalline silicon particles from sample Di-ex with (a) a part of the agglomeate, (b) a zoom into that region and (c) the appropriate diffraction pattern.

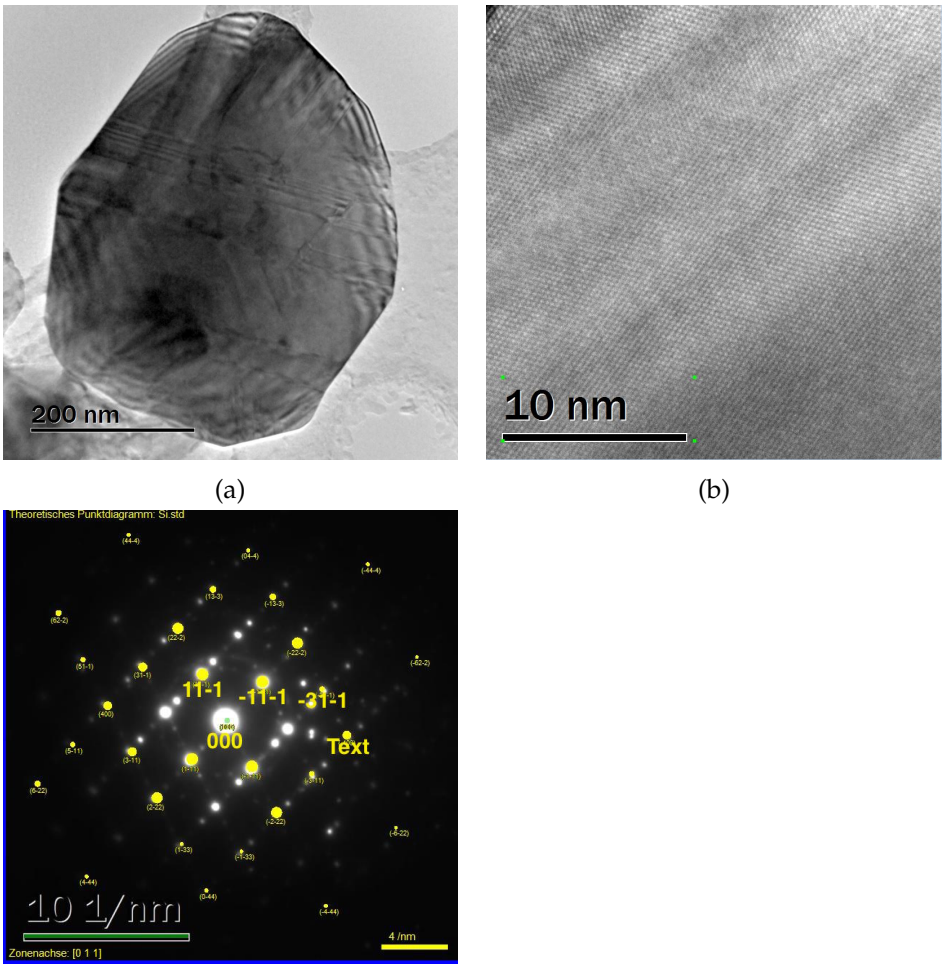

(a) (b)

(c)

Figure 3.41: TEM image showing a silicon single crystal from sample Di-ex, where (a) the whole crystal shows, (b) a HRTEM image of that particle and (c) the appropriate SAD pattern.

Figure 3.40a shows a part of this agglomerate and 3.40b and 3.40c show the magnification of this and the appropriate diffraction pattern, respectively.

One mentionable feature is one, in comparison, large single crystal that was observed in this specimen. In figure 3.41 an overview of the particle is shown together with a high resolution image and the diffraction pattern. The high resolution image shows a crystal lattice free of any faults such as twins. However, in the lower magnification image 3.41a such lattice defects can be observed. In the SAD pattern a tripling of the spots is visible. Here, the main diffracted beams have a weaker second and this one an even weaker third spot beside them.

Figure 3.42 shows the result of the EDS measurement from sample Di-ex. Beside the expected Si also elements such as C, Cu and O were observed. As stated before Cu and O are from the sample holder and the exposure to air. The C detected in this sample supposedly comes from the

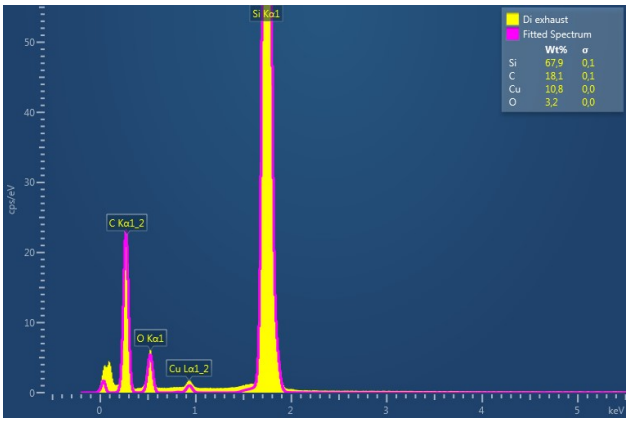

Figure 3.42: EDS result of sample Di-ex.

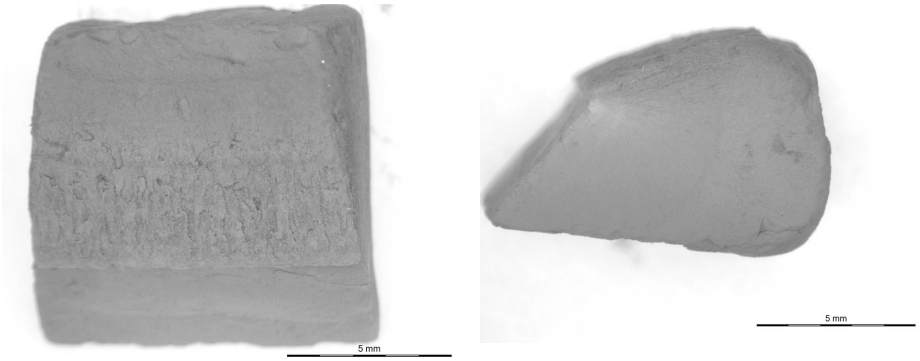

(a) (b)

Figure 3.43: Stereo microscopic image of sample Dc-w-b with: (a) view on top of the material and (b) the side view.

holey carbon of the sample holder.

3.2.2 Sample Dc

Out of the second batch from the Dynatec reactor two significantly different samples were taken. Both samples are from the reactor; sample Dc-w-a comes from the upper part whereas sample Dc-w-b is from the lower part.

Sample Dc-w-a shows a material that is very light, spongelike and soft. It can easily be scratched or crushed and has to be handled with great care. As it can be seen in figure 3.43 the specimen is homogeneous, no layered structure can be seen. In fact, the porosity is so high, that reasonable images could not be taken with help of the reflective light microscope.

SEM images from sample Dc-w-a, presented in figure 3.44, show, just as the visible light microscope, a homogeneous structure through out the whole material. There are no layers nor cracks visible. The high porosity is very well seen in the images. As it can be seen in figure 3.44b the structure looks such as if it consists of spheres, less than 1 μm in size, that appear to

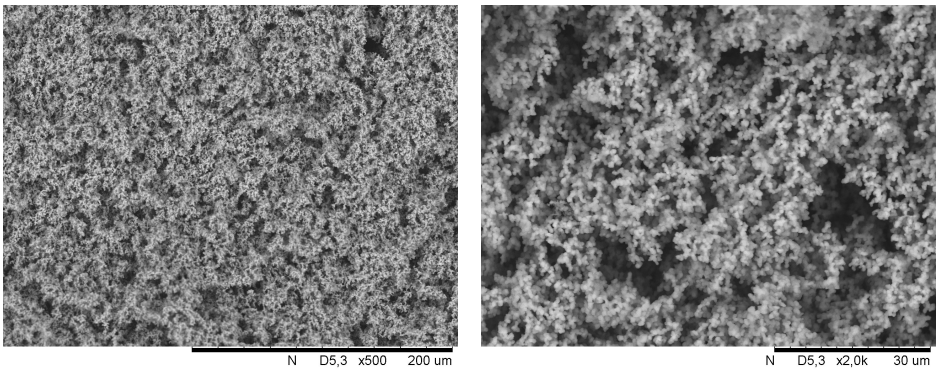

(a) (b)

Figure 3.44: SEM images of sample Dc-w-a.

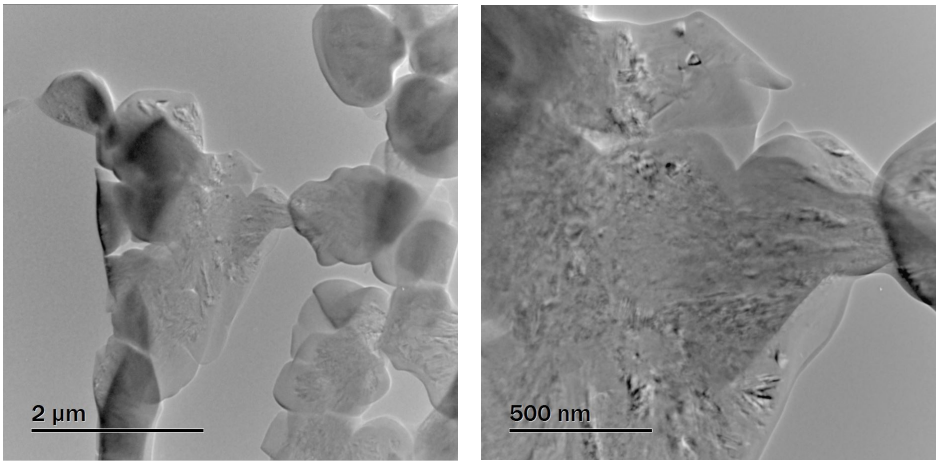

(a) (b)

Figure 3.45: TEM images of sample Dc-w-a.

have grown together. However, it appears that the spheres grow together rather in beads than tightly packed, hence the high porosity.

The highly porous material from sample Dc-w-a also showed crystallinity throughout the specimen. Figure 3.45 shows an overview image and one detail image. It appears that the particles did not grow together very tightly as it has been suggested previously.

Figure 3.46 presents the high resolution and FFT image of sample Dc-w-a. A lattice without defects can be seen.

In figure 3.47 the result of the EDS measurement can be seen. It shows there are, beside the expected Si, other elements from the environment such as Cu from the sample holder, O from the oxidation of the specimen due to contact with air and Ar due to the ion milling in the sample preparation process.

In figure 3.48 sample Dc-w-b is shown from two different directions. Figure 3.48a is an image from the region close to the wall. This is the

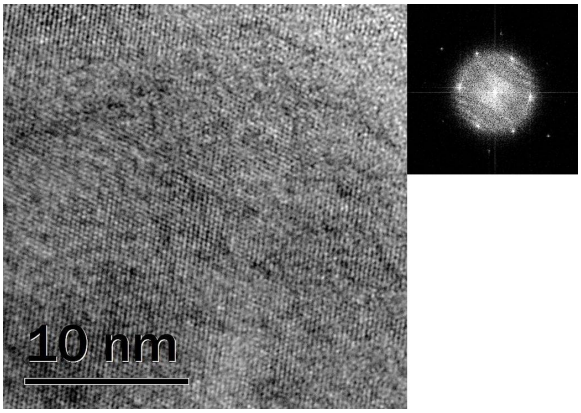

Figure 3.46: HRTEM and FFT image of sample Dc-w-a.

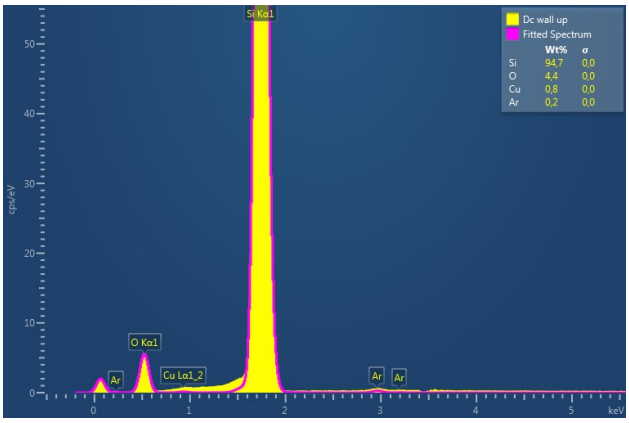

Figure 3.47: EDS measurement of sample Dc-w-a.

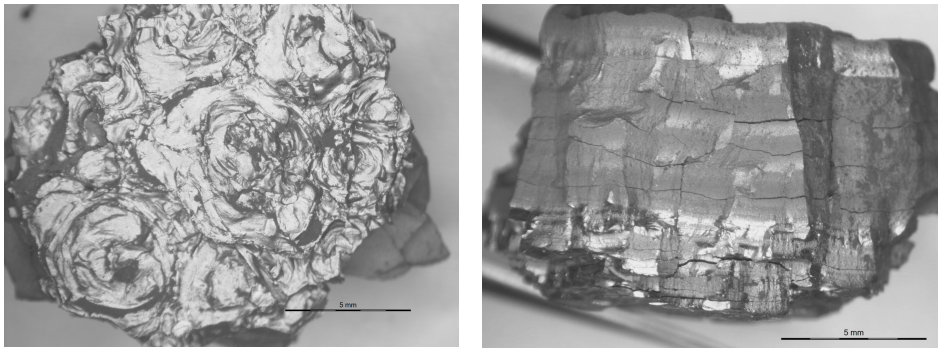

(a) (b)

Figure 3.48: Stereo microscopic images of sample Dc-w-b with: (a) side towards reactor wall and (b) side view.

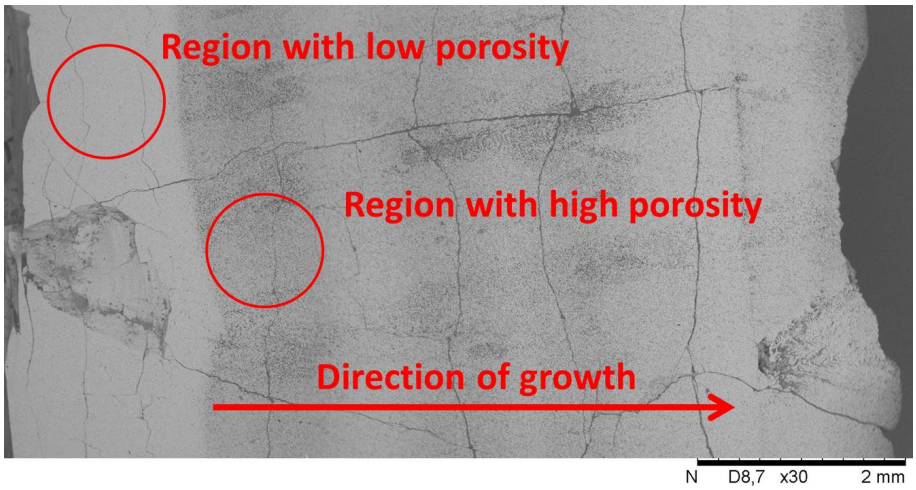

Figure 3.49: EDS measurement of sample Dc-w-a.

material growing in the beginning of the process. Due to the fact that this sample is very brittle and full of cracks (figure 3.48b) it is assumed that the part which can be seen in the image is not directly from the wall. This part is very shiny and reflective. However it seems to be built up in round flakes, such as rosettes, that easily fall off when touched. This kind of structure had approximately 2 mm in thickness and was followed by a less reflective texture. Figure 3.48b presents the different structures of the material, where the flake-like, shiny part is on the bottom and the less reflective throughout the rest of the material. Clearly visible is the layer-like built up of the material, representing chronologically the production process and possible changes in the process parameters. Interesting feature in this sample are the cracks that are normal to the growth direction. They mostly follow in the direction of the layers and are the main reason for brittleness of the material. As in the previous crystal from sample Di showed, the side facing the reactor wall had fine powder on top. The surface appears dark grey and porous. The material is, however, so hard that is not easy to scratch.

As it already has been shown in visible light images, there are some significant differences between sample Di and Dc. With help of SEM the differences become more obvious and clear.

In sample Dc-w-b a clear layer structure is evident. Also visible are the many cracks through the material mainly in direction parallel to the layers. Figure 3.49 clearly shows both features.It is noticeable that most crevices parallel to the layers go through darker, and thus more porous regions.

In higher magnification the micro structure of the layers becomes visible. It is apparent that the brighter parts show a lower porosity. Figure 3.50a is from an area with a porosity as low as 6 %. This material was grown in the beginning of the process. Figure 3.50b appears to be more porous. It was produced later in the process and has a porosity of more than 50 %. average measurements resulted in a porosity of 6 to 11.6 % for the dense material and 36 to 55 % for the porous material.

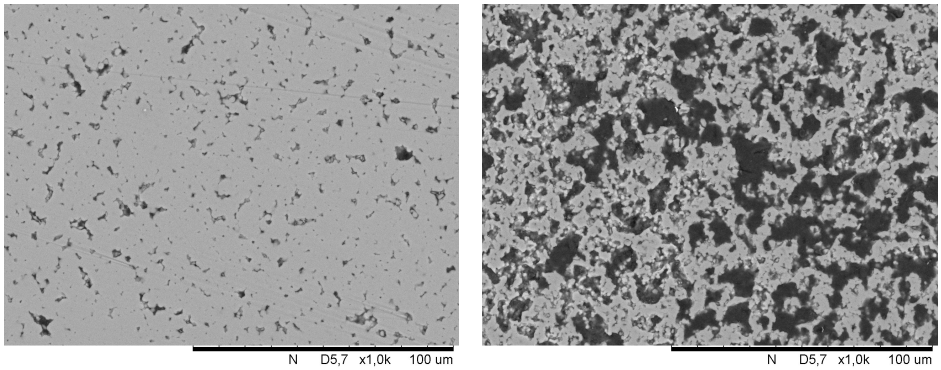

(a) (b)

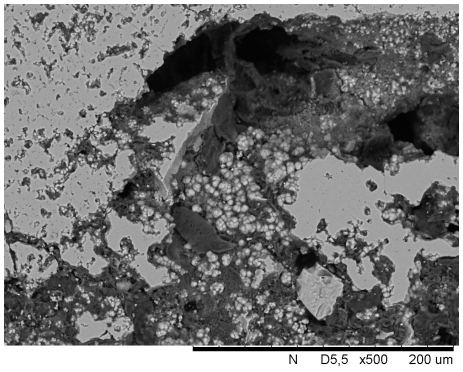

(c)

Figure 3.50: SEM images of sample Dc-w-a in high magnification with: (a) low- and (b) high porosity. Image (c) shows a growth defect in close up.

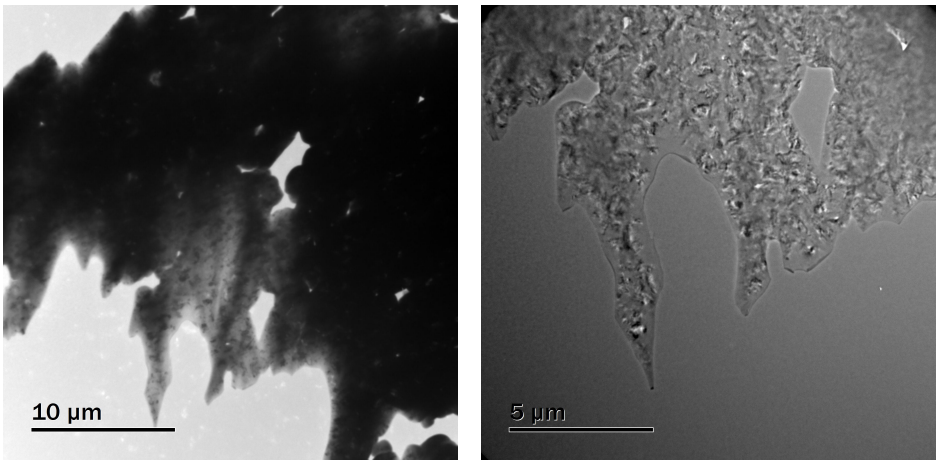

(a) (b)

Figure 3.51: TEM image of sample Dc-w-a showing an overview over a section which is analysed nearer.

In figure 3.50c a growth defect is magnified (which also can be seen in figure 3.49). Eye-catching is this defect as it gives an insight into the unpolished bulk material. The image shows small spheres grown into each other. These spheres are a few μm in diameter.

Figure 3.51 gives an overview of an area of sample Dc-w-b. In image 3.51b it can be seen that the material is crystalline. Amorphous areas seen around the edges of the material result from ion milling in the preparation process.

A closer look into the material shows several spherical particles grown together (figure 3.52). The images show the polycrystallinity of the particles (3.52b) and the different orientation of each particle (3.52d).

A few crystals were observed big enough to show the diffraction pattern of the material properly. Such a particle can be found in figure 3.53. The SAD pattern seen in image 3.53c again shows a tripling in the spots.

The EDS result from sample Dc-wb shows a small content of carbon beside silicon, which is expected. The elements such as Copper, Oxygen and Argon are due to the sample holder, air contact and sample preparation.

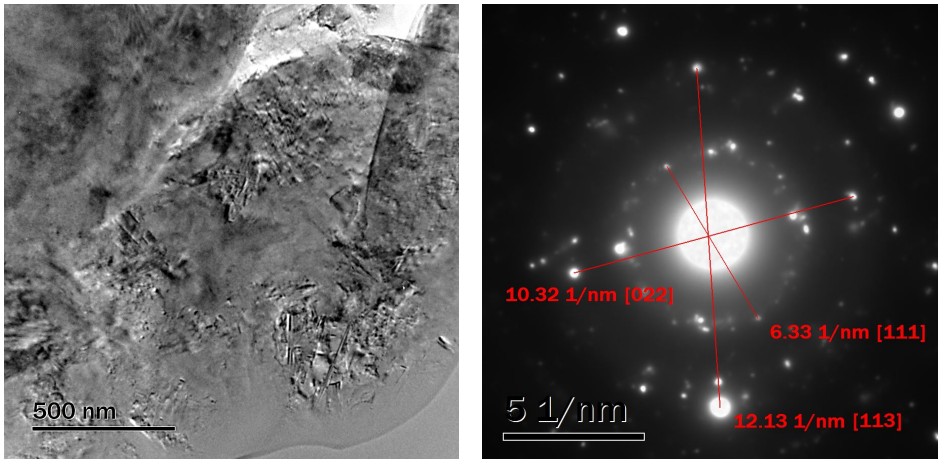

(a) (b)

(c) (d)

Figure 3.52: TEM images of a particle including the diffraction pattern (b), the bright field- (c) and dark field image (d).

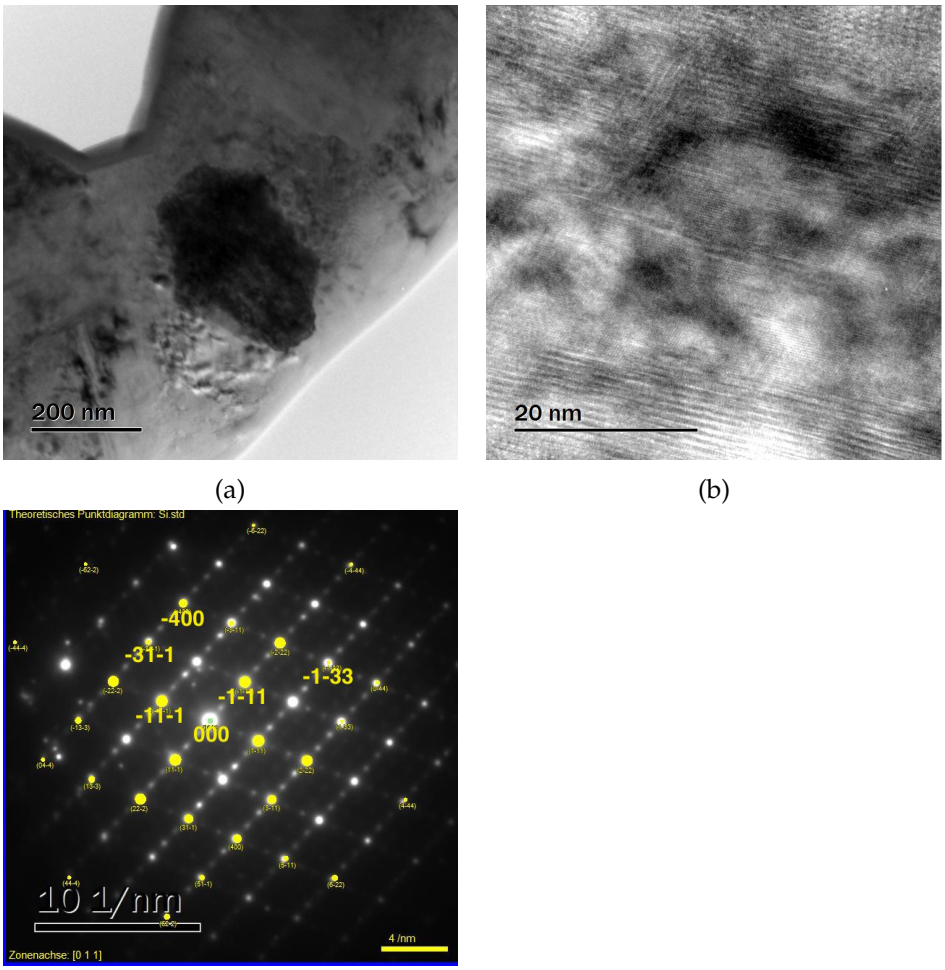

(a) (b)

(c)

Figure 3.53: TEM image of sample Dc-w-a with a bright field image (a) and the corresponding high resolution image (b) and diffraction pattern(c).

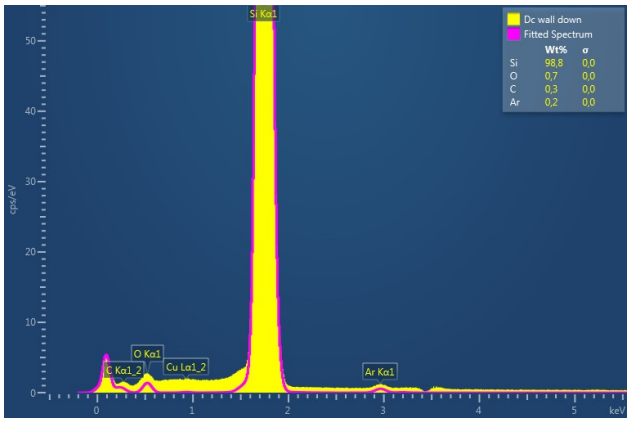

Figure 3.54: EDS measurement of sample Dc-w-b.

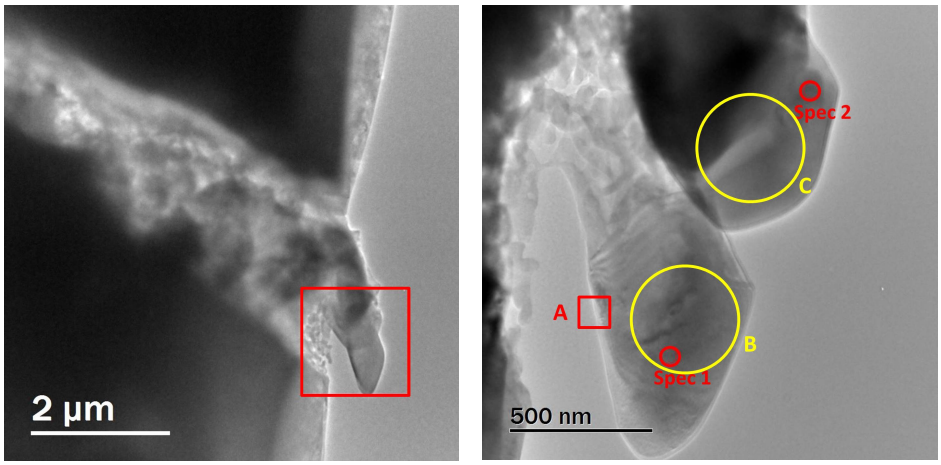

(a) (b)

Figure 3.55: TEM image showing the location of the particles and the exact point where EDS measurements were performed. Image (b) is the same location but a different tilt angle than image (a). The areas indicated with letters point out where FFT (A) and SAD (B and C) were performed.

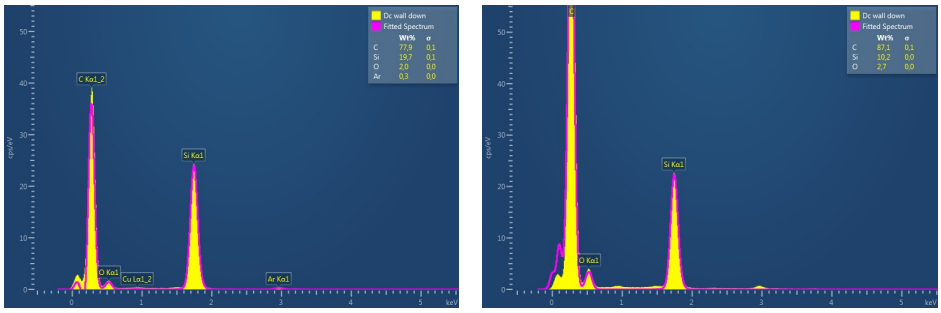

(a) (b)

Figure 3.56: EDS measurements of the two particles indicated in image 3.55 as Spec 1 for (a) and Spec 2 for (b).

One interesting artefact was found in sample Dc-w-b showing massively different EDS measurements. Figure 3.55 shows the location of the particles in question. As it can be seen in image 3.55a the particles are at the end of a crevice. They appear to be single crystals.

As seen in the images in figure 3.56, both crystals have a very high content of Carbon with about 77 % and 87 % respectively. The silicon content is approximately 20 % and 20 % respectively. The rest is Oxygen, which is expected to come from the exposure to air.

It appears that several carbon structures can be found on the two crystals. The first structure was observed in the area marked in image 3.56 with the red letter A. Figure 3.57 shows a HRTEM image with a FFT taken from the marked square. The FFT image suggest a graphite structure.

Figure 3.58 shows two SAD patterns from two locations of the

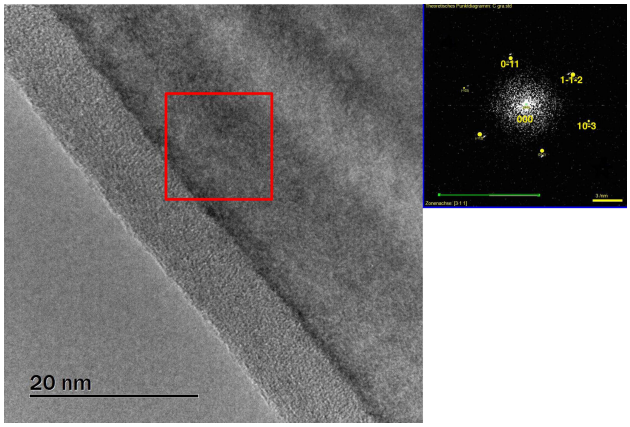

Figure 3.57: High resolution TEM image of the area marked with A in image 3.56. The FFT is from the red frame of this image.

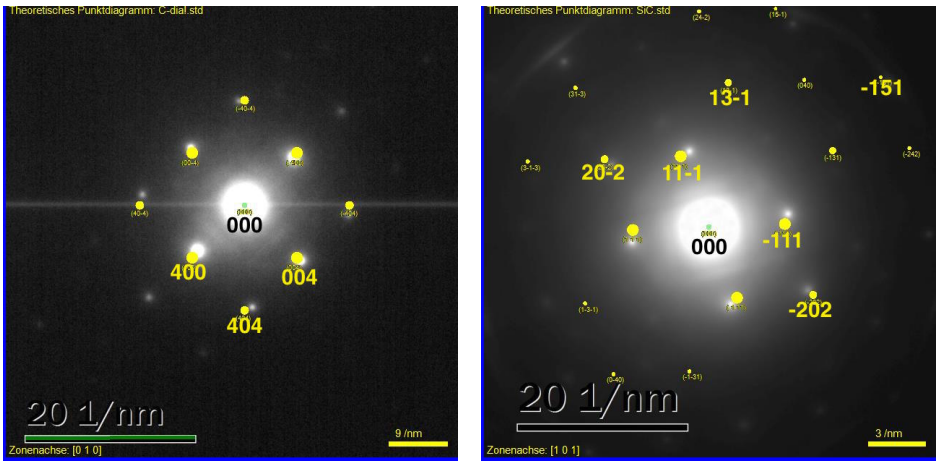

(a) (b)

Figure 3.58: SAD pattern from sample Dc-w-b, from two carbon rich particles.

crystalline particles seen in figure 3.55. Image 3.58a was recorded in the area marked with a yellow B. Image 3.58b comes from the area marked with the yellow C. The SAD pattern from image (a) appears to be a crystalline carbon structure in the [010] zone axis. Image (b) on the other hand shows the SAD pattern from a SiC crystal in the [101] zone axis.

4. Discussion

In this project ten silicon samples have been studied using various microscopy, diffraction and spectroscopy methods. The samples originate from two different, newly developed reactors, the Free Space Reactor (FSR) and the Dynatec Centrifuge Reactor (DCR). The material from the FSR differs in terms of process parameters such as temperature, and chemistry, as some samples have been in-process doped with phosphorus. The DCR samples originate from two batches, with different temperatures and other unlike conditions. The samples of the two batches also differ in terms of the exact location where that were taken from within the reactor.

As it can be seen is the variety of samples quite big. The comparability, however, is not always given. In this chapter the results that have been described previously are discussed.

4.1 Free Space Reactor

4.1.1 Particle growth in the Free Space Reactor

The general functionality of the FSR has been explained in the introduction of this work. However, what happens within the reactor in detail has not been pictured. As described, the gas is flowing through the tube in a non chaotic, laminar way. That means that the particles have a different retention time in the heating zone, as the flow velocity is higher in the middle of the reactor. Hence, the duration in which the silicon particles are in the heating zone is different. This means in detail that particles passing the reactor through the centre are in contact with the heating zone for a shorter time and exposed to a lower temperature. The particle which passes through the heating zone close to the wall on the other hand stays in the heating zone a longer time at higher temperatures. Assuming that the concentration of silane is the same throughout the reactor diameter that would mean a growth of bigger particles close to the wall. When taking into account that the reactor runs at the lowest possible temperature to reduce the energy usage, it means that the particles in the centre of the reactor tube possibly do not get enough kinetic energy to form a crystalline structure. The concentration of silane is, however, not the same throughout the reactor diameter. This is on one hand due to the velocity and temperature gradient and on the other hand because the inner

tube, where the reactions happen, is porous with inert gas flowing into the reaction chamber avoiding the attachment of silicon to the tube. For the particle production it has the consequence that relatively more small particles are produced that are possibly rather amorphous. The particles are expected to be smaller because they have a relatively higher velocity that close to the wall. More particles are produced because of the higher silane concentration, since hydrogen is flowing through the perforated wall. Lastly, a higher amount of amorphous particles expected as the temperature is lowest in the middle. These effects might be small, but when running the reactor at the lowest possible temperature to reduce total energy consumption, they are possibly decisive.

The particle growth has been described by [15] as a diffusion driven process, where, in a system below the melting temperature, the diffusion happens on the surface. The growth starts after decomposition of the material when the system is supersaturated. Initially two Si atoms, now no longer bound to the hydrogen, come in contact and combine. Others join as the particle grows. While the particle is growing it comes in contact with other particles and they grow together. Since a sphere is the most energy efficient shape the particle tries to become spherical by means of diffusion. Is the temperature where this particle grows high enough, a crystalline structure is developed; otherwise it is amorphous. The particle grows as long as it is in a zone where the temperature is high enough. No spheres were found that have visible pores.

4.1.2 Laminar flow

It was often observed that the crystalline particles consisted of nanocrystals, i.e. a sphere where the crystalline structure throughout the sphere has many different orientations. This indicates the proof of the growth process described above.

An interesting observation during the analysis of all samples is that the particles from the FSR reactors were all found to be in agglomerates. The agglomerates are built up from spheres that are connected to each other in shapes that look like beads. All agglomerates were either amorphous or crystalline; however, none of the two combined. This, and the fact that the agglomerates mostly contain similar seized spheres, suggest that the particles that form the agglomerates stays in the same diametric area throughout the heating zone. This in turn confirms the assumption that the flow through the reactor is laminar.

4.1.3 The powder samples without phosphorous doping

Sample Fi600 is the material from the FSR with the highest process temperature. According to [28] the decomposition temperature of monosilane is 420 °C. At this temperature, however, the created material is amorphous as the kinetic energy is not sufficient to form crystalline structures ([10]). Thus, by raising the temperature, the amount of crystalline particles in the

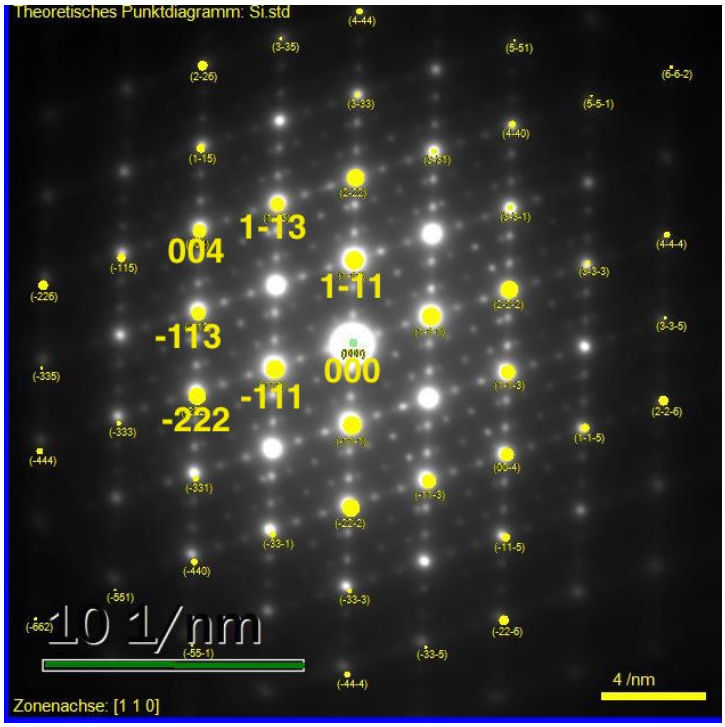

Figure 4.1: SAD image of sample Fp525 showing a tripling in the diffraction pattern.

end product will increase. This can be seen by comparing figure 3.2 and 3.6 where the plots from sample Fi600 and Fi575, respectively, show the distribution of particles size and content of amorphous and crystalline agglomerates are presented. As conditions other than temperature are supposed to be constant, the difference can be explained with the increased temperature.

Another difference between the crystalline particles from these two samples is that Fi600 shows a nanocrystalline structure whereas Fi575 shows a crystal with lattice defects but nonetheless all the same directions. However, no statistical relevant information about this has been obtained.

4.1.4 Tripling in the SAD pattern

A feature seen in sample Fp525 is the tripling of spots in the SAD pattern, as it can be seen in figure 4.1. A possible cause is the precipitation of phosphorous phases in silicon. In figure 4.2 the Si-P phase diagram can be seen. It appears that Si has no solubility of P at room temperature. At process temperature, however, Si has a solubility of less then 1 %. But since the content of P in Si is higher than 1 % it can be assumed that a SiP phase is present. Olesinski et al. mentions in the explanation of the P-Si phase diagram a reported metastable Si_2 P phase which was produced from a mixture of silane (SiH_4) and phosphine (PH_3) at 450 °C [29]. These precipitations might cause lattice defects such as twins, where the ordinary

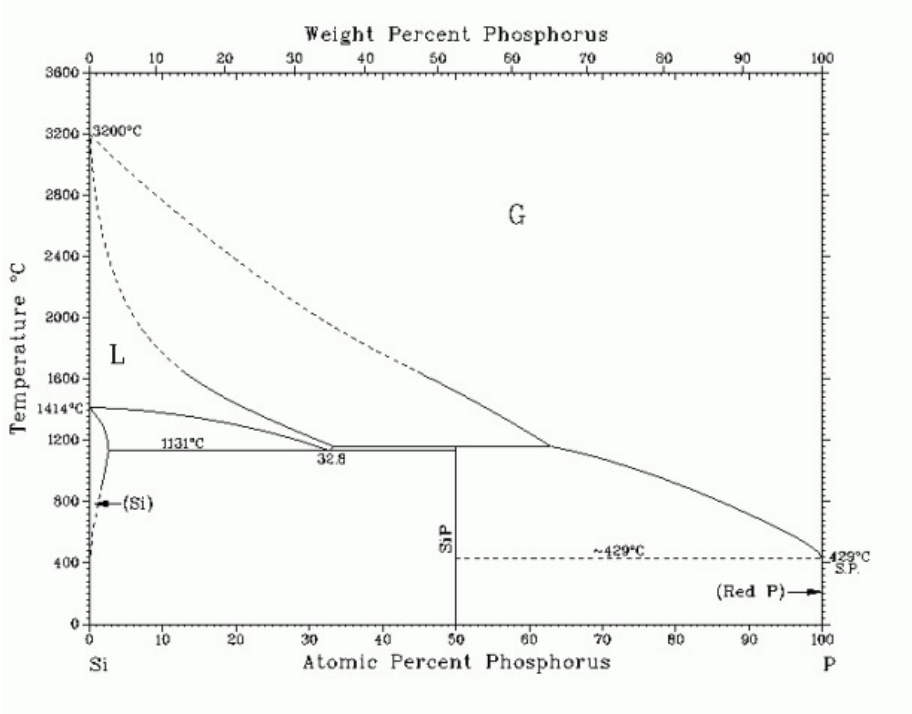

Figure 4.2: Si-P phase diagram [29].

build up of the lattice is interrupted, and hence result in the tripling. The tripling is a result of a second lattice that creates a new reflection opposite of the centre beam.

SiP has an orthorhombic crystal structure. However, the reflexes seen in the diffraction pattern do not fit in with the reflexes of that phase. This is another indication that the SiP phase is not the source of the tripling. Yet, the tripling of the SAD pattern presented has also been observed in sample Di-ex which is free of any doping or contaminating elements. Thus it can be concluded that the tripling of the SAD pattern is presumably due to twin formation.

4.1.5 The influence of the phosphorous doping and the XRD results

Sample Fi575 and Fp525 show very similar results when it comes to particle size distribution and the XRD experiment result. In both samples a distribution of the particle size could be found, where the major part of the particles had a size between 50 and 200 nm. The greatest part of the counted particles appear to be amorphous. Also, the XRD results from both samples have the same features. Figure 3.11, page 26, and figure 3.7, page 24, show the plot with the XRD results for sample Fp525 and Fi575 respectively. Clearly visible are the peaks at 28° and about 52°. The shoulder seen in at about 15° is due to the PMMA-sampleholder (it can be observed in all XRD results) [30].

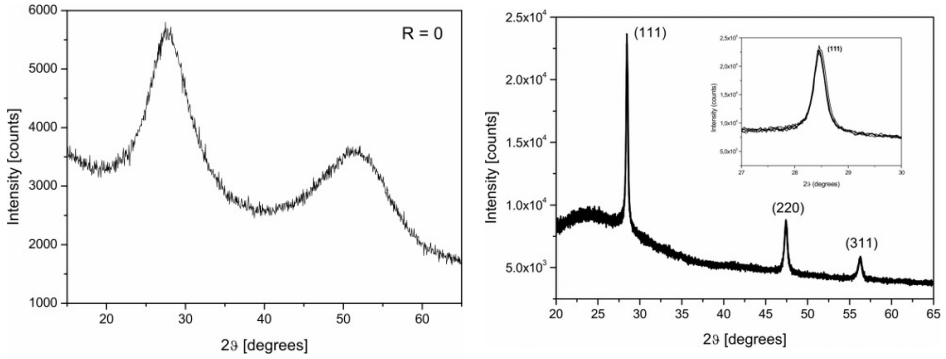

(a) (b)

Figure 4.3: XRD pattern of amorphous hydrogenated (a) and crystalline silicon (b) [33].

A feature of XRD analysis is, beside the determination of the crystal structure, also the measurement of the crystallite size. Crystallites are individual perfect crystals; they can form single-crystals or poly-crystals. Jones discusses the method for measuring the size [31]; the author describes a broadening of the peak when the crystallite size is smaller than about 100 nm. Yet, Tomaszewski argues in his paper that a precise grain size can not be calculated from XRD data [32]. By using the first peak at about 28 ° the crystallite size has been determined for sample Fp525 and found to be 16 Å. Due to great similarity in the XRD result a number very close to this is assumed for sample Fi575 as well. These results are contrary to what has been found by the particle count. An explanation might be that the crystallites measured are with 1.6 nm very small, so that they might occur amorphous at magnification at which the agglomerates were counted and the size of the spheres determined, typically x=100.000 to x=250.000. Sphere size is the measure of the silicon particles from the reactors, most of such particles have a spherical shape. Crystallite size on the other hand is the size of grains within the material. In these grains the crystal structure is free of defects.

Vavrunkova et al. et al studied the recrystallization of amorphous silicon films [33]. In their work amorphous hydrogenated silicon has been has been heated up to temperatures between 580 and 620 °C in order to crystallize the silicon. Plots of their XRD measurements can be seen in figure 4.3. As it can be seen are the graphs for the amorphous and crystalline material very similar to the results presented in this thesis. Especially the amorphous plot is in contrast to what has been stated before, but it supports on the other hand the counting of the amorphous and crystalline particles done with the TEM. In addition it is plausible to expect the amorphous powder to be amorphous hydrogenated silicon, as it has been used by Vavrunkova et al. et al. Hydrogen passivation of silicon has been studied [34]; since the newly produced silicon powder is exposed to Hydrogen at all time, it can be assumed that it has been passivated.

It is interesting that Fi575 and Fp525 is so similar, because the process

temperature is 50 °C lower for the sample doped with phosphorous. A possible reason might be due to the P-doping in sample Fp525. It has been reported that the growth rate of silicon increased when the deposition material was doped with phosphorous [35] [36]. For that reason it is suggested that due to the doping of phosphorous similar conditions for the formation of silicon particles exist at 50 °C lower than for the material with out P.

This hypothesis is supported by the samples Fp575a and Fp575b. Both powders show clear peaks suggesting that their average particle size is significantly larger. Assuming the same conditions inside the reactor except for the presence of P (i.e. particles velocity, temperature, pressure, among others) suggests that the particles grew quicker in the same time frame. In addition the plots of the measured size of the particles show that sample Fp575a has bigger particles compared to Fi575 (figure 3.15, page 28, and figure 3.6, page 24 respectively). Another indication is the shape of the XRD plots of both samples as they can be seen in figure 3.7, page 24, for sample Fi575 and in figure 3.16, page 29, for sample Fp575a. The relation between particle size and broadening of the peak in the XRD plot appears to be distinct. It can be assumed that the P content is the reason for that.

Comparing the high resolution images of sample Fi575 (figure 3.8, page 25) and Fp575a (figure 3.17, page 29) shows two different growth mechanisms. The analysed particle from sample Fi575 show an epitaxial grown structure of a single crystal, containing lattice faults such as twins. The image from sample Fp575a on the other hand shows a particle containing several grains that have grown together. The extent to which the results can be generalized from these two images is questionable. Firstly because both particles might originate from two different locations within the reactor tube where they where exposed to different velocities, temperatures and silane concentrations. Yet stronger evidence for the lack of representativeness are the results of the XRD measurements stated before.

Since the sample Fp575b is the comparison check for Fp575a to verify the continuity of the process, both samples are supposed to have same process conditions and thus the same results. Figure 3.17, page 29, and figure 3.22b, page 31, show high resolution images of both samples. It appears that both materials have a rather similar crystalline structure consisting of nanosized crystallites. Sample Fp575a shows this in the FFT images of figure 3.17 taken from several spots of the presented image. Sample Fp575b on the other hand shows in the appropriate SAD image a poly crystalline pattern beside the spots of the $\langle 022 \rangle$ view. This implies that both samples have an alike crystal structure. Supported is this supposition by the XRD results shown in figure 3.16 on page 29 and figure 3.20, page 31. Despite different height of the peaks due to significant lower counts per second in the latter sample, it can be assumed that both samples have similar features in terms of crystallinity and crystallite size as both samples show sharp peaks but yet a significant broadening at the bottom of the peak.

4.2 Dynatec Centrifuge Reactor

4.2.1 Sample Di-w-a, Di-r and Di-ex

The samples Di-w-a, Di-r and Di-ex all originate from the same batch of the Dynatec reactor. The differences lie in the location within the reactor and thus the certain process parameters change. Sample Di-w-a was collected from the wall of the reactor. This sample was a dense, hard crystal with clear shape as it can be seen in figure 3.24 on page 32. Sample Di-r was from the ceiling, it is a light, porous material which appeared to be very unstructured. On the side towards the reactor centre, this material shows a surface that seems to be shaped by a gas flow (figure 3.32, page 36). The last sample is Di-ex, a powder that was captured in the exhaust (figure 3.38, page 40).

Since, in this type of reactor, the wall is the only heat source it can naturally be assumed that sample Di-w-a is subjected to the highest temperature. In addition to that, it can be assumed that the centrifugal forces close to the wall are higher than in any other location in the reactor. This again leads to the conclusion that the material from this part has the highest density, which appears to be true.

The material from the ceiling is much lighter and brittle. The surface looks, as mentioned, as if it was shaped by a gas flow. An explanation for that can be found in the geometry of the reactor, where the silane and hydrogen gas mixture enters the reactor in the bottom and is pressed against the wall due to centrifugal forces (that are normal to the wall). It should be mentioned that due to the higher mass of the silane gas molecule it is pressed against the wall with a higher force than hydrogen and hence pushing it to the reactor centre. Nonetheless, the gas rises along the wall to the ceiling and leaves the reactor through the exhaust.

It is proposed that the mentioned shapes of sample Di-r are created by the stream of gas passing by the ceiling on the way to the exhaust. Hereby some particles are carried with the gas stream together with the remaining silane that has not been decomposed. The particles get stuck on the ceiling and grow together in an uncontrolled manner with help of the remaining silane. Both the reduced temperature and changed force conditions (perpendicular to the ceiling) support the hypothesis that a less dense material is formed. The reduced temperature reduces the diffusion speed and the force is no longer pressing the silicon together. It is assumed that the shape of the material is created when small particles 'hide' behind bigger ones or get stuck due to turbulences and thereby creating a bigger obstacle for following particles. It is evident that particles stream towards the exhaust due to the simple fact that there are particles in the exhaust. The spherical shapes that are suggestively visible in the SEM images on page 38. A possible explanation is that these spheres were formed around powder particles such as those marked in figure 3.34c.

The EDS measurement from this sample shows very unexpected and inconclusive results. Two results are shown in figure 3.37, page 40. The

first image shows the result from an amorphous particle. It proves to be pure silicon, besides Copper and Oxygen from the sample holder and the exposure to air, respectively. The second measurement was made on polycrystalline material of the same sample. It shows strange elements such as Calcium, Sulphur, Iron and others. The origin of these elements is uncertain. There were several measurements performed with several samples and different preparation methods, yet all the crystalline material shows a variety of elements whose origins were not conclusively proven. This is in accordance with the SAD pattern from figure 3.36. While the amorphous sample appears to be silicon, the amorphous rings of the [111] and the [113]-type reflection are clearly visible, so can the diffraction pattern from the polycrystalline sample not be assigned to silicon.

The sample captured from the exhaust was a fine powder. Figure 3.38, page 40, shows the powder; in the stereo microscopic image it can be seen that there are grains of different sizes. A closer look with help of SEM unveils nonetheless, that the powder grains themselves consist of much finer particles (figure 3.39 on the same page). Due to the fine consistency the particles easily stick together. Since the powder managed to escape the reactor chamber, despite the rotational forces, suggests that they are very light rather than compact. This in turn suggests that they do not consist as much of spheres as other less dense particles geometries.

As it can be seen three very different kind of materials were found in the reactor, depending on the location. The crystal structure of these samples changed from crystalline structure on the wall, to partly crystalline and amorphous on the ceiling and mostly amorphous with only few crystalline particles in the exhaust.

The micro structure from sample Di-w-a develops when the particles form in the gas phase. The particles grow into spheres much like what happens in the FSR. Yet then they are forced to the wall and sinter together with other particles. Thus a dense material can be found with a fine polycrystalline crystal structure. In TEM images the outlines of spheres can be seen (figure 3.28b, page 34). SAD pattern and high resolution TEM images on page 35 show that the lattice is largely free of stacking errors. This could be seen as a hint for a homogeneous growth, because the sphere grows continuously adding silicon atoms that follow the lattice structure the way it started. Another possible explanation is that, while the particles grow, some others attach and they grow together. One structure, however, dominated and overgrew the others and with high enough temperature in place the overgrown lattice switched to the dominating structure to reduce the tension within, created by grain boundaries.

As stated has sample Di-r both amorphous and crystalline parts. Figure 3.35, page 38 shows both types, where the amorphous are big, flake-like and rather transparent and the dark appearing, smaller particles that are crystalline. Previously it was suggested that lighter particles were carried by the gas flow to the ceiling and got stuck there to grow into the light and porous material that can be found. In this regard the amorphous particles seem to be rather flat and thus in a not good surface to volume

relation. It could be due to their shape that they are caught by the flow more easily then other particles. The crystalline particles however appear very small which might be the reason for them to be transported there. It seems like they have a very fine crystallinity which supports the theory that they first got trapped on the ceiling and then grew together with other similar particles. Since, however, the temperature is reduced on the ceiling, the crystalline particles still grow together but they do not form a single crystal structure. The remaining silane in the gas mixture works, following this hypothesis, as a glue holding together the small crystals.

The powder captured from the exhaust showed for the greatest part amorphous particles. Yet a few crystalline particles were found. The material found in the exhaust had to overcome the major obstacle of the rotational force. To achieve this it had to stay in an area where this force is smallest, which is the centre. Since, in the gas phase, silane is relatively heavier that the hydrogen, the latter one is forced to the centre of the reactor. For the particles, this has the consequence that they can not grow any further. Assuming they do not leave the centre means that they will, carried by the hydrogen, leave the reactor through the exhaust. As the temperature in the centre and thus furthest from the heat source, is lowest, the predominating amorphous structure of the particles are easily explained. The crystalline silicon could either come through the same path, or by the gas stream that passes by the solidified silicon.

4.2.2 Sample Di-w-a versus Dc-w-a

Comparing sample Di-w-a and Dc-w-a, both originate from the same spot in the reactor, shows significant differences in the macro- and micro structure. The known differences from the process are both a slightly lower process temperature and carbon contamination in the latter sample. When studying the materials it is clear that there are few similarities.

When studying the materials, differences were significant even before analysing the with microscopes. While sample Di-w-a was a dense, crystal-shaped and hard material, so was Dc-w-a very light, very porous and so soft that it could be crushed without the lightest effort. This can be seen in figure 3.24, page 32, and figure 3.43, page 43, for sample Di-w-a and Dc-w-a respectively. In these pictures, it also is eye-catching that only Di-w-a shows the seed particles that are inserted into the reactor to make it easier to remove the finished material. The reason for that is open for speculation. One suggestion is that due to the very soft material the sample simply broke of and did not stick with the particles. However, the later discussed material Dc-w-b does not show these particles either, so that it might be due to the production conditions of this batch specifically. Sample Dc-w-a appears to be very homogeneous throughout the whole material. Both VLM and SEM images show that there are no significant artefacts within the bulk material (page 43). Sample Di-w-a on the contrary shows a structured crystal with different amount of voids throughout the sample. The seed particles appear to have very few voids with a measured

porosity of 6.6 % to 10.7 %. The material around the particles proves to be very porous as it can be seen in both VLM and SEM images on page 32, measurements show an approximate porosity of 37 %. The material that follows has again a reduced porosity of 12 to 16.4 %. The porous layer between the seeds and the not so porous bulk can be seen in image 3.27a on page 34.

The creation of the pores might be due to the following scenario: At the beginning of the process only the seed particles are inside the reactor, fixed to the wall due to centrifugal forces created bz the rotation of the reaction chamber. After introducing the silane gas it decomposes and precipitates as soon as the environment is oversaturated. At this point silicon particles are created in a supposedly similar manner as in the FSR: firstly the Si atoms link with each other in a nucleation process and then they grow because other atoms attach to them, or other nuclei link with them so that they grow together. This happens wherever the temperature is high enough, which is close to the wall. The silicon particles are at all times exposed to the centrifugal force and thus they are pressed against the wall where they grow together and form a solid layer, which is the end product. However, as the particles that are being pressed against the wall have a rather spherical shape (cf. image 3.28b, page 34, the spherical shape of particles viewed under a TEM) they often produce voids that can not get filled with silicon because other particles close the contact to the gas phase.

In regards of the porous layer next to the seed particles, following thoughts might be considered as an explanation. Since the wall is the heat source for the reaction, it is assumed that the temperature is highest near the wall. This means that diffusion processes take place quicker the closer the material is to the wall. It is also assumed that diffusion below the melting temperature is along the surface as suggested by Giesen [15]. In the case of sample Di-w-a this means that the material close to the wall is during the whole process diffusing, under the influence of the centrifugal force, in direction wall. The porosity of the layer next to the seed particle suggest that from this area, the silicon diffused towards the wall to build up a more dense layer.

The outstanding V-shapes close to the wall, around the seed particles are, however, not yet explained. So far no research has been done if the seed particles, that are in the reactor, change the size during the process [37], yet the previous paragraph suggests that they grow. In image 3.26a, page 34, it appears as if the silicon grows in arms out of the particles. A possible explanation is that the first produced particles get attached to the sides of the seed particle, blocking the further way towards the wall. The next sphere touches the previous one a little further outside and a little further from the wall and thus creating the V-shape. Figure 4.4 shows a schematic drawing of this explanation.

Considering, however, that this is a 3 dimensional material would imply that the 'arms' in fact are cones formed around the tip of the seed particle. Further research e.g. with Computer Tomography imaging could deliver deeper information.

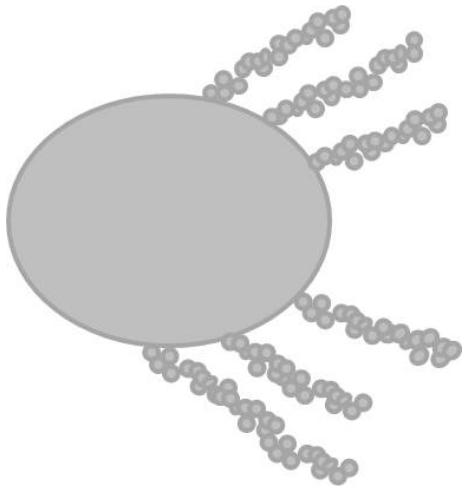

Figure 4.4: Drawing of the possible growth from the seed particle.

A V-shaped feature can also be seen in the bulk material in figure 3.27b, page 34. The feature seen appears to be a growth fault creating a big void; the size of which is approximately 100 μm in length and 10 μm in depth. Assuming that all silicon particles segregate from the gas phase at a more or less same size suggest that the cause for the fault is not a big particle. More realistic is a bit by bit coincidental growth of silicon spheres around a volume and hereby creating the void.

Another scenario assumes that the reactor is subjected to forces such as vibrations, with 1000 rotations per minute [21] this is very realistic. It could be that a particle from the ceiling has been loosened by these vibrations and was then forced against the wall by the centrifugal forces. This would create a void. The fact that there are several voids on what looks like the same layer suggests that a particle broke in several artefacts.

Sample Dc-w-a shows a micro structure that is very different from the one of sample Di-w-a. As previously explained is this specimen very soft and light. In figure 3.44, page 44, the SEM images of this sample is seen. It is obvious that this material is by no means as dense as sample Di-w-a. The structure of the material appears to be build up by spheres into beads that are interconnected. The network of the small spheres appears entirely random. Comparing sample Dc-w-a with sample Di-w-a suggest that the temperature difference and the mentioned carbon contamination resulted in a entirely different growth mechanism. Though this suggestion presumes that no other process parameter was changed and the conditions for the experiment were unchanged.

A possible explanation can be that the critical temperature for extensive diffusion was not reached in sample Dc-w-a. This hypothesis is supported by the highly porous material compared to Di-w-a. As it is assumed that conditions such as the rotation speed are constant, the force, that acts on the particles, is also the same. As mentioned, sample Dc-w-a is supposed to be carbon contaminated. However in the tested specimen no carbon was

found, as figure 3.47 on page 45 shows. Whether this is due to small sample volume or lack of carbon, it should be investigated further.

TEM images of both samples show crystalline structure. In fact, the images showing the whole crystals look quite alike as it can be seen in image 3.29a, page 35, for sample Di-w-a and image 3.45b, page 44, for sample Dc-w-a. The amorphous edge around the particles is due to ion milling the sample preparation process. The high resolution images of both samples show error free structures with no apparent lattice faults such as twinning. Although statistical information about such a fault in this material has not been gathered, it can be suggested that the conditions in which the particles were produced (in the gas phase) are very similar.

4.2.3 Comparison of the carbon contaminated Dynatec samples

The two samples from the second batch out of the Dynatec Centrifuge Reactor showed very different structure and allow a view into the mechanisms within the reactor chamber. As described above has sample Dc-w-a a homogeneous yet sponge-like and soft material. Sample Dc-w-b on the other hand is hard, brittle and has a layered structure. While it is very dense in the region close to the reactor wall it gets more porous after 2 to 3 mm. The dense layer show a flake-like shape, when seen from the wall the flakes look like a rose.

Figure 3.49, page 46, shows that throughout the material cracks can be seen. As their predominant direction is parallel to the layers and that they can be found throughout the whole material it is plausible that they occur after the process was finished. This suggests that they formed when the reactor cools down which in turn means that they are due to shrinking of the material. In sample Dc-w-a this was not observed, which means that a minimum porosity is required. However, neither in the dense, carbon free sample Di-w-a such cracks were observed which indicates a connection to the carbon content. Possible explanation is that the carbon prevents a homogeneous contraction of the silicon and thus increase the creation of cracks.

The layers visible in cross section in figure 3.49 are due to the changing porosity. What, however, changed in the process that suddenly a higher porosity is being produced is open for speculation as no further information was given. Possible may be changing parameters such as reduced silane content. No such changes can be observed in sample Dc-w-a though, which suggest that such changes did not occur. Thinkable is also that the thickness of the silicon layer is the reason for the sudden increase in porosity. The assumption is that the thermal conduction of the material is such that after a certain thickness, the thickness of the dense layer, not enough heat arrived to support as much diffusion as in the beginning. The argument against this thought is that firstly no other sample showed this behaviour and secondly is the rest of the sample more or less homogeneous in the porosity but it probably should show gradually higher porosity.

A not yet discussed topic is the structural difference between sample Dc-w-a and Dc-w-b. Since they are from the same batch, they are produced under the exact same conditions. The only difference is the gradually reduced content of silane in the gas mixture along the wall going from high content at the bottom to low content close to the ceiling. Due to the higher silane content at the bottom supposedly more and bigger silicon particles are produced from the gas phase. This hypothesis is supported by Images from both samples. Image 3.44b, page 44, shows a SEM image of sample Dc-w-a at x=500 magnification where the fine particles are visible. Sample Dc-w-b on the other hand can be seen in image 3.50c, page 47. The view into a void reveals the size of particles this material in build up with. The magnification of both images is the same.

4.2.4 The role of carbon in the Dc-w samples

The carbon appears to be unequally distributed throughout the system. EDS measurements show no carbon in the specimen from the top of the wall (figure 3.47, page 45). Another picture is drawn, however, at the bottom of the wall, where Dc-w-b was taken from. The results in figure 3.54 show a small peak indicating the presence of carbon in the material, below 1 wt.%. Nonetheless, particles were found that contain a much greater amount of carbon, where a different carbon structures were observed, as figure 3.55 and the following show. The first particle show a carbon content of more than 77 wt.% and the second about 87 wt.% C. The different carbon structures detected were graphite and crystalline carbon (on the particle that says Spec 1, figure 3.56b, page 51), and SiC on the second particle (Spec 2). It is surprising that the particle with a lower carbon content shows pure carbon structures, whereas the one containing more carbon shows SiC. To form SiC one Si and one C atom is needed. There is approximately 9 times as much carbon than there is silicon. Since the values are given in wt.% and the silicon is more than twice as heavy as carbon, it can be assumed that roughly 90 % of the carbon is not bound by the silicon. Such compounds are graphite or crystalline carbon.

In figure 4.5 the C-Si phase diagram can be seen. It can be seen that there is no solubility of Si and C into each other. That means, that as soon as carbon comes into the silicon lattice, SiC is formed and vice versa. For the here discussed sample it means that as long as there are both elements present they will form SiC. Published literature mentions temperatures of as low as 400 °C [39]. Since the reactor runs at higher temperatures anyway, this is not a limiting parameter.

Interesting and worth mentioning is, that the carbon rich particles were found at the beginning of a crevice as it can be seen in image 3.55a. More investigation is, however, needed to determine if this is coincidence or if the carbon is accumulating at such locations.

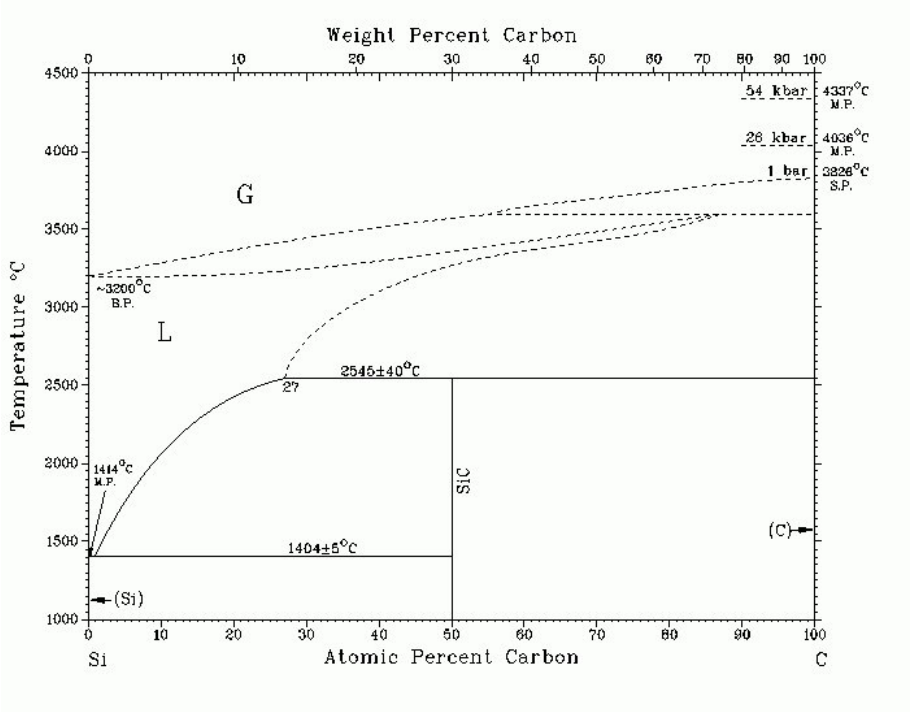

Figure 4.5: C-Si phase diagram [38].

4.3 Further results

The EDS results obtained by measurements in the TEM are exposed to inaccuracies and errors. Sources for such limits can be e.g. not representative samples or contaminations. A common danger is that weak peaks are covered by background noise and thus not visible. Also, overlapping peaks could make the read-out difficult. Accuracies better than $\pm$ 1 % (relative) are obtainable for abundant elements, but overall accuracies are commonly near $\pm$ 2 % [40]. This means for the results obtained in this project, that the measured elements in generals are present in the sample, but the exact measured amount is to be taken with caution.

5. Conclusions

In this thesis samples from the Free Space Reactor and the Dynatec Centrifuge Reactor, two novel CVD rectors for silicon production, were investigated and the presented results were discussed.

The Free Space Reactor

The particles are spherical in shape. They stick together to form agglomerates and the agglomerates are either amorphous or crystalline. That means that no major turbulences occur inside the heating zone during the production process. Thus it can be said that the gas flow is laminar. The formation of crystalline or amorphous particles is, to some degree, depending on the diametric location of the particles.

The size of the particles is, among other parameters, depending on the temperature. A higher temperature results in bigger particles. Increased temperature also leads to more crystalline particles. The greatest part of the particles was in the size range 50 - 200 nm. Only the Powder produced at 600 °C showed predominantly particles that were 200 nm and larger.

The use of Phosphorous as a doping element can reduce the critical temperature to produce crystalline particles. Using Phosphorous resulted in a higher content of crystalline particles compared to powders produced at the same temperature without Phosphorous. P-doped particles showed the same characteristics as not doped particles at production temperature 50 °C lower than for the not doped.

Particles form by the coalescing of smaller particles. By means of diffusion they merged to become spherical. If the temperature is high enough, the crystal lattice of the whole particle will align with the dominating direction. This way an energetic, more favourable structure is acquired.

XRD is a helpful tool in determine the crystallinity of a powder. However, to determine if a powder is nanocrystalline or amorphous, the help of other methods is necessary. TEM is in this context very useful.

By comparing the XRD results with published literature, it can be said that silicon particles have been passivated by the hydrogen environment.

The Dynatec Centrifuge Reactor

Depending on the location where specimens were taken from has a major impact on crystallinity, density and brittleness of the product.

The silicon from the wall is mainly crystalline, whereas samples form the ceiling are partly crystalline, partly amorphous and the material from the exhaust almost only amorphous.

The material on the wall grew by spheres that were pressed against the wall by means of centrifugal forces. The spheres accelerate towards the wall and sinter together with surrounding material. Hence the polycrystalline structure. Near the wall, the temperature is the highest so the diffusion process is the quickest which leads to the most dense material produced.

It is assumed that the silicon from the ceiling grew under the influence of a far weaker force, as the material is very porous and light. Here, the main source for silicon are particles that are drawn to the ceiling by the gas flow and deposit together with remaining silane. Due to the cooler ceiling, this silicon is partly amorphous.

The powder found in the exhaust consists of very small, light particles. They originate from the centre of the reactor, where the centrifugal forces are minimal, and exited the reactor with the exhaust. It is mostly amorphous as it has never been close to the heating source.

The silane content of the reaction gas decreases as it decomposes, rises and flows towards the ceiling and the exhaust. That influences not only the deposition speed, but also the product quality.

Carbon contamination resulted in an unequal distribution of Carbon throughout the sample. It has been found that it influenced the homogeneous growth and led to a diverse end product. While there were parts where no Carbon has been found whatsoever, other locations showed high C content of up to 87 wt.%. The carbon formed SiC, graphite and crystalline C structures.

Other

Twinning in the crystal structure has often been observed. It was shown that it appeared independent from the composition of the material. Twin occurrence resulted in a tripling of the SAD pattern, where additional reflexes appear between the primary pattern.

Future work

- Better (larger) statistic for counting the crystal type and size.

- further investigation of sample Di-r to clarify the composition that is not explainable at this point.

- Further work is needed to understand how the change of silane content within the DCR changes the deposition of Si along the wall towards the ceiling.

- A closer collaboration with IFE with more direct feedback could mean a huge step forward and enhance fruitful development.

Glossary

λ wavelength of incident radiation.

BSE backscattered electrons.

C Carbon.

cf. confer, lat.: compare.

CT Computer Tomography imaging.

Cu Copper.

CVD Chemical Vapour Deposition.

d distance between two lattice planes.

DCR Dynatec Centrifuge Reactor.

DP diffraction pattern.

e.g. exempli gratia, lat.: for example.

ED electron diffraction.

EDS electron energy dispersive spectroscopy.

FBR Fluidized Bed Reactor.

FSR Free Space Reactor.

H Hydrogen.

HCl hydrochloric acid.

HRTEM high-resolution transmission electron microscopy.

i.e. id est, lat.: that is.

IEA International Energy Agency.

IFE Institute for Energy Technology.

n integer.

O Oxygen.

PMMA Poly(methyl methacrylate).

PV Photo Voltaic.

SAD Selected Area Diffraction.

SE secondary electrons.

SEM scanning electron microscope.

Si Silicon.

SiC silicon carbide.

SiO_2 silicon dioxide.

TCS trichlorosilane.

TEM transmission electron microscope.

v.i. vide infra, lat.: see below.

VLM visible light microscope.

XRD X-ray diffraction.

Bibliography

[1] P.A. Cox. *The Elements: Their Origin, Abundance, and Distribution*. Oxford science publications. 1989.

[2] *Chinas swift solar PV market dominance*. URL: http://cleantechnica.com/2012/09/07/eu-launches-wto-investigation-into-chinese-silicon-pv-dumping-allegations/.

[3] *Price history of silicon PV in $ per watt*. digital image. URL: http://commons.wikimedia.org/wiki/File:Price_history_of_silicon_PV_cells_since_1977.svg (visited on 21/04/2015).

[4] José M. Martínez-Duart and Jorge Hernández-Moro. 'Commentary: Photovoltaics firmly moving to the terawatt scale'. In: *Journal of Nanophotonics* 7.1 (2013), pp. 078599–078599.

[5] *private communication*. 18th Apr. 2015.

[6] M. Kirkengen. *IFE-Akademiet "Fra Lima til Paris". Norges og IFEs rolle i å redusere verdens CO2-utslipp*. Presentation. Institute for Energy Technology, 16th Apr. 2015.

[7] *Photovoltaic Supply Chain*. URL: http://www.sneresearch.com/tit_img/200412.jpg.

[8] *The Photivoltaics Value Stack*. URL: http://www.greenrhinoenergy.com/solar/industry/images/Prices%20and%20Cost-04.jpg.

[9] Jafar Safarian, Gabriella Tranell and Merete Tangstad. 'Processes for Upgrading Metallurgical Grade Silicon to Solar Grade Silicon'. In: *Energy Procedia* 20.0 (2012), pp. 88 –97.

[10] Werner O. Filtvedt. 'Production of polisilicon from silane pyrolysis in fludized bed'. PhD thesis. Telemark University College, 7th June 2013.

[11] C. S. Herrick and D. W. Woodruff. 'The Homogeneous Nucleation of Condensed Silicon in the Gaseous Si-H-Cl System'. In: *Journal of The Electrochemical Society* 131.10 (1984), pp. 2417–2422.

[12] C. H. J. v. d. Brekel F. C. Eversteyn P. J. W. Severin and H. L. Peek. 'A Stagnant Layer Model for the Epitaxial Growth of Silicon from Silane in a Horizontal Reactor'. In: *Journal of the Electrochemical Society: Solid State Science* (1970).

[13] T.U.M.S. Murthy et al. 'Gas-phase nucleation during the thermal decomposition of silane in hydrogen'. In: *Journal of Crystal Growth* 33.1 (1976), pp. 1 –7.

[14] Karl A. Kusters and Sotiris E. Pratsinis. 'Strategies for control of ceramic powder synthesis by gas-to-particle conversion'. In: *Powder Technology* 82.1 (1995), pp. 79 –91.

[15] B. Giesen. 'Modellierung und Simulation der Synthese von Nanopartikeln in der Gasphase'. PhD Thesis. Universitaet Duisburg-Essen, 18th Oct. 2005.

[16] *Siemens Process*. URL: http://www.thequartzcorp.com/en/blog/2014/04/28/polysilicon-production/61.

[17] V. Revankar and S. Lahoti. 'CVD-Siemens Monosilane Reactor Process with Complete Utilization of Feed Gases and Total Recycle'. Pat. 2012.

[18] *Granular Polysilicon Technology*. 17th May 2012. URL: http://www.recgroup.com/Global/section_img/REC_Granular%20polysilicon%20Technology_170512.pdf.

[19] W.O. Filtvedt et al. 'Development of fluidized bed reactors for silicon production'. In: *Solar Energy Materials and Solar Cells* 94.12 (2010), pp. 1980 –1995.

[20] *Growth regimes of polysilicon from gaseous precursors*. 23rd Sept. 2013.

[21] W.O. Filtvedt and J. Filtvedt. 'Reactor and method for production of silicon by chemical vapor deposition'. Pat. Apr. 2013.

[22] S. Amelinckx et al. *Handbook of Microscopy, Handbook of Microscopy: Applications in Materials Science, Solid-State Physics, and Chemistry. Methods II*. Handbook of Microscopy. 2008.

[23] *electron interaction with matter*. URL: http://www4.nau.edu/microanalysis/microprobe-sem/signals.html.

[24] *Crystallographic Planes in Si*. 1998. URL: http://jas.eng.buffalo.edu/education/solid/unitCell/home.html.

[25] *Bragg's law*. URL: http://pd.chem.ucl.ac.uk/pdnn/powintro/diffrac.gif.

[26] *Web Electron Microscopy Applications Software*. URL: http://emaps.mrl.uiuc.edu/emaps.asp.

[27] A. R. West. *Solid State Chemistry and Its Applications*.

[28] Y. Q. Liu Y. J. Liu. 'The Industrial Research about China Solar PV Based on the Price of Polysilicon'. In: *Advanced Materials Research 383-390* (2011).

[29] R. W. Olesinski, N. Kanani and G. J. Abbaschian. 'The PSi (Phosphorus-Silicon) system'. In: *Bulletin of Alloy Phase Diagrams* 6.2 (1985), pp. 130–133.

[30] Armel Le Bail et al. *Powder Diffraction*. Ed. by R E Dinnebier and S J L Billinge. 2008.

[31] F. W. Jones. 'The Measurement of Particle Size by the X-Ray Method'. In: *Proceedings of the Royal Society of London. Series A, Mathematical and Physical Sciences* 166.924 (1938), pp. 16–43.

[32] P. E. Tomaszewski. 'The uncertainty in the grain size calculation from X-ray diffraction data'. In: *Phase Transitions* 86.2-3 (2013), pp. 260–266.

[33] V Vavrunkova et al. 'Study of re-crystallization processes in amorphous silicon films'. In: *Microelectronics Proceedings (MIEL), 2010 27th International Conference on*. 2010, pp. 257–260.

[34] U. Hansen and P. Vogl. 'Hydrogen passivation of silicon surfaces: A classical molecular-dynamics study'. In: *Phys. Rev. B* 57 (20 1998), pp. 13295–13304.

[35] R. Bisaro et al. 'Solid-phase crystallization kinetics in doped *a*-Si chemical-vapor-deposition films'. In: *Phys. Rev. B* 31 (6 1985), pp. 3568–3575.

[36] SP Murarka and TF Retajczyk Jr. 'Effect of phosphorus doping on stress in silicon and polycrystalline silicon'. In: *Journal of Applied Physics* 54.4 (1983), pp. 2069–2072.

[37] *private communication*. 23rd May 2015.

[38] R. W. Olesinski and G. J. Abbaschian. 'The CSi (Carbon-Silicon) system'. In: *Bulletin of Alloy Phase Diagrams* 5.5 (1984).

[39] Qingyi Lu et al. 'Growth of SiC nanorods at low temperature'. In: *Applied Physics Letters* 75.4 (1999).

[40] *Introduction to Energy Dispersive X-ray Spectrometry (EDS)*. URL: http://cfamm.ucr.edu/documents/eds-intro.pdf.